Perfusion-Rate Estimation Using Ultrafast Speckle-Decorrelation Ultrasound Imaging

by

Mayara Nascimento de Oliveira

A thesis submitted in partial fulfillment of the requirements for the degree of

Master of Science

in

Biomedical Engineering

Department of Electrical and Computer Engineering
University of Alberta

Abstract

Estimating tissue perfusion has great clinical applications such as the prediction of anti-angiogenic therapies and stroke management. Ultrasound perfusion imaging is preferable than other methods since it has real time capabilities, and it is inexpensive. The method proposed in this study shows the relationship between tissue perfusion and speckle decorrelation rate when high-frequency, high-frame rate ultrasound is used. We also investigated the use of lower frequency ultrasound transducers with high-frame rate, plane wave compounding imaging, and the results are promising. This new approach to estimate tissue perfusion waves the need for contrast agents while providing quantitative information on tissue perfusion (consequently, outperforming PD imaging) as well as morphological information. We combined adaptive block-wise SVD filter, AM2D algorithm for tissue motion compensation and Golay sequences to substantially increase the SNR and therefore increase perfusion sensitivity with the ultimate goal of proving the robustness of this new method and its capability to being used in clinical applications.

Preface

This thesis is an original work by Mayara Nascimento de Oliveira.
The introduction in Chapter 1, the background information in Chapter 2 and the conclusion in Chapter 5 were strictly done by the author.
The research including the simulations and *in vivo* experiments were conducted together with my colleagues Tarek Kaddoura, David Egolf, Quinn Barber, Min Choi, Pradyumna Kedarisetti, and the essential guidance of Dr. Roger Zemp.
As the lead author I was responsible for implementing the algorithm used to calculate the speckle-decorrelation rate, as well as implement (based on previous studies) the complex tissue filters used in this issue, including the second-order SVD filter, adaptive block-wise SVD filter and the high-order SVD filter. Furthermore, I was responsible for implementing the Golay sequences for the Verasonics Vantage system.
The simulations were done together with Tarek Kaddoura, David Egolf and Quinn Barber. *In vivo* experiments were performed with the assistance of Min Choi and Pradyumna Kedarisetti.
Dr. Zemp advised me throughout the whole process giving input on what was most relevant for this study and assisting me with thesis writing.

Acknowledgements

First and foremost, I would like to show appreciation for my supervisor Dr. Roger Zemp who believed in me and gave me the opportunity to pursue a Masters degree at the University of Alberta. Thank you for all your encouragement and for setting the standards high.

To my parents, I am extremely grateful for all the sacrifice you guys made to ensure I could finish this degree. The last few years were not easy, but allowed us to strengthen our bond and improve our relationship. I truly love you mom and dad, this degree goes to you and it is an honor to be the first person on our family to receive a masters degree from an institution outside of Brazil.

To my colleagues, thank you for all the support and for the amazing work done before my time in the lab that allowed me to stand on your guys' shoulders.

To my friends in Canada, you are my family. Thank you for the encouragement and for being with me during the whole time. I would not be able to finish this thesis without your support, thank you for teaching me what perseverance is about.

Table of Contents

List of Figures

List of Symbols

Below is a list of frequently used symbols along with their general meaning to aid the reader.

- p_0 – Initial Induced Pressure
- k – Material Compressibility
- Δf – Transducer Bandwidth
- c – Speed of Ultrasound
- Z – Acoustic Impedance
- α – Attenuation coefficient
- f – Frequency of the Transducer
- α_o – Temperature Dependent Factor of Attenuation
- n – Material Parameter
- θ_i – Angle of Incidence
- θ_t – Angle of Transmission
- ci – Speed of Sound in the Incident Medium
- ct – Speed of Sound in the Transmitted Medium
- θ_{cr} – Critical Angle
- R – Reflection Coefficient
- T – Transmission Coefficient
- ε_{HbO_2} – Oxyhemoglobin extinction coefficient
- ε_{Hb} – Deoxyhemoglobin extinction coefficient
- $\Gamma(x)$ – relative Gruneisen parameter
- $\phi(x, \lambda_k)$ – wavelength dependent fluence

Glossary of Terms

Below is a list of frequently used terms along with their general meaning to aid the reader.

- CT – Computed Tomography
- SPECT – Single Photon Emission Tomography
- MRI – Magnetic Resonance Imaging
- PET – Positron Emission Tomography
- LDF – Laser Doppler Flowmetry
- US – Ultrasound
- sO_2 – Blood Oxygen Saturation
- MRO_2 – Rate of Oxygen Consumption
- PD – Power Doppler
- CEUS – Contrast-enhanced Ultrasound
- SNR – Signal-to-Noise Ratio
- PA – Photoacoustic
- HbO_2 – Oxyhemoglobin
- HbR – Deoxyhemoglobin
- FDA – Food and Drug Administration
- SA – Synthetic Aperture
- GPU – Graphical Processing Units
- FPGA – Field Programmable Gate Array
- CNR – Clutter-to-noise Ratio
- MB – Microbubbles
- HI – Harmonic Imaging
- ROI – Region of Interest

- RF – Raw Radio-frequency Signal
- RBC – Red Blood Cells
- SNCR – Signal-to-noise + clutter Ratio
- FOV – Field of View
- BOLD – Blood Oxygen Level Dependent
- EPRI – Electron Paramagnetic Resonance Imaging
- PWC – Plane Wave compounding
- SVD – Singular Value Decomposition
- HOSVD – High-order SVD filter

Chapter 1

Introduction

1.1 Motivation

The main goal of the circulatory system is to provide cells with oxygen and nutrients and remove products, such as carbon dioxide, from tissue [9,19]. This exchange takes place in small vessels called capillaries that connect arterioles with venules [9] and estimating the efficacy of this transport mechanism is of great clinical value [9,25].

However, estimating blood flow in a single capillary is a challenge since its diameter varies from 5μm to 200μm [8]. Fortunately, this is not an important parameter to evaluate the efficacy of the microcirculatory system, instead, it is more important to focus on the amount of blood supplied to a tissue [9]. This is called blood perfusion and it is defined as the blood volume flowing through a unit volume of tissue per second (ml/(cm^3.s)) [1,9,19]. In other words, it corresponds to the total amount of blood flowing through the microcirculatory system in a tissue, *e.g.*, muscle, tumors, placenta or brain.

Perfusion imaging also provides important information to assess a variety of physiological processes, either normal or pathological, that are related to the changes in blood perfusion [25]. For instance, diseases such as diabetes and cancer, show changes in microvasculature [8,14]. Specifically, in oncologic diseases, an increase of vasculature around a tumor (angiogenesis) is an important indicator of tumor aggressiveness, and can indicate a difference between a malignant or benign cancerous growth [4], or be related with subsequent metastasis [18]. With current oncologic treatments focusing on

controlling angiogenesis [8,14], perfusion imaging techniques are important not only for diagnosing, but also for treatment monitoring [6,7,15,18]. Furthermore, estimating perfusion is a promising tool to discriminate between cancer and inflammation [26], since a relative increase in blood perfusion is observed in soft tissue inflammation [25].

Several non-invasive imaging modalities can be used to quantify tissue perfusion, such as single photon computed tomography (SPECT), multidetector computed tomography (CT), magnetic resonance imaging (MRI), and positron emission tomography (PET). Nevertheless, these techniques are expensive, and expose the patient to radiation or nuclear tracers, limiting their popularization [1,8].

Laser Doppler Flowmetry (LDF) is another non-invasive technique that provides continuous measurement of tissue perfusion [9,19,27]. In this case, laser light is scattered by moving red blood cells, which, according to the Doppler effect, causes a frequency shift that can be detected [9]. Nevertheless, this technique has a limited penetration depth (0.5mm to 1mm), therefore, it is mostly used to detect skin perfusion [9,19], even though advances in data processing to increase signal-to-noise ratio (SNR) can lead to increasing measurement depth.

Ultrasound (US) perfusion imaging is preferable than previous methods since it has real time capabilities, it is relatively inexpensive, and it is non-ionizing and non-invasive [1,4,8,9,26]. Moreover, in comparison with LDF it provides a larger penetration depth [9,19].

However, there are some limitations related to conventional US, for instance, images are often of poor quality and suffer from many artifacts (attenuation) [26]. Furthermore, the demands to measure perfusion are higher than the ones to measure flow in large vessels [9], and therefore, conventional Doppler and

Color Doppler US systems, which are widely used to estimate blood flow in large vessels [28], may not be suited for this application.

For instance, the low velocity in which red blood cells are moving in the microcirculatory system (0.1 to 10mm/s) [1,3,8], results in small Doppler frequency shifts and consequently a good frequency resolution is needed [9]. Additionally, conventional Doppler US systems operating at 2-10MHz do not provide sufficient spatial resolution to image vessels in the microcirculatory system [1,3,8] and the US system needs to have a good SNR, so that the weak signal backscattered from blood in microvascular structures can be distinguished from clutter [8,9].

To overcome the above problems, it is possible to inject brighter ultrasonic scatterers, often gas-filled microbubbles, in the vascular system [3,8,14]. Therefore, enhancing the intensity and contrast of the signal backscattered from blood, and improving sensitivity [2,3,4,5,7,8,14]. Despite that, microbubbles are only approved by FDA for use in certain cases such as echocardiology and radiology [34].

This thesis proposes primarily the use of high frequency ultrasound, which automatically enhances the resolution and increases the backscattering coefficient of blood and a speckle tracking technique to estimate blood perfusion. Also, we propose the use of ultrafast ultrasound to increase the ensemble size and consequently increase the signal-to-noise + clutter ratio. Low-frequency ultrasound using diagnostic frequencies was also used with the designed algorithm and results were promising.

Furthermore, using the estimation of blood oxygen saturation (sO_2) one can also estimate the rate of oxygen consumption (MRO_2), which is important for studying tissue metabolism and diseases related to oxygen metabolism such as diabetes [29,30]. Combining the proposed method to estimate blood perfusion

with photoacoustic signals for estimation of sO_2 leads to estimation of oxygen metabolism which is also proposed in this work.

1.2 Key Contributions

This thesis investigates the potential of ultrasound and photoacoustic signals for estimating blood perfusion rates along with oxygen metabolism.

Compared to other techniques for estimating tissue perfusion, ultrasound is a better option since it is inexpensive and has a scalable penetration depth. Nevertheless, conventional US techniques used to estimate blood flow in large vessels, such as Doppler ultrasound, are not well suited to obtain information about the low blood flow in microcirculation. To increase blood scattering coefficient, it is possible to use microbubble contrast-agents or high-frequency ultrasound systems.

Power Doppler (PD) images combined with high-frequency ultrasound systems and advanced clutter filtering techniques has shown a significant improvement in perfusion sensitivity and provide information about microcirculation morphology in many organs. Nonetheless, this technique lacks information about blood speed and therefore it is not possible to estimate perfusion quantitatively which is a disadvantage compared to contrast-enhanced ultrasound (CEUS) and other non-invasive techniques.

To fill that gap this work proposes the use of speckle tracking methods. Those methods were first proposed to overcome limitations of conventional Doppler ultrasound [19]. Echo signals backscattered from blood and tissue can be tracked since they behave in a pattern that remains relatively constant as blood or tissue moves. Nevertheless, to the best of our knowledge, no one has proposed the use of a speckle-tracking technique to generate perfusion mapping images and provide quantitative measurements of tissue perfusion.

The first contribution hence demonstrates the use of high-frame-rate ultrasound imaging, which has been employed on detecting subtle blood flows by tracking flow at thousands of frames per second, combined primarily with high-frequency (diagnostic frequencies were also addressed) US systems where the echogenicity of blood is significantly higher than at low diagnostic frequencies. Furthermore, we propose the use of Golay excitation combined with block-wise SVD filter and the AM2D algorithm for tissue motion compensation to increase SNR, and consequently increase perfusion sensitivity while preserving resolution.

The second and final contribution is to use photoacoustic (PA) imaging to determine sO_2 (multiwavelength PA measurements were used to determine the sO_2 defined as the ratio of oxyhemoglobin concentration ($[HbO_2]$) to total hemoglobin concentration ($[HbO_2] + [HbR]$)) and consequently MRO_2 when combined with the speckle tracking technique proposed.

Accordingly, this work introduces a new method for estimating perfusion using high-frequency, high-frame-rate ultrasound imaging by estimating speckle decorrelation rate that when combined with PA imaging will be able to estimate oxygen metabolism in the future.

1.3 Layout of Thesis

This thesis is organized as follows: Chapter 2 will provide a background and literature review of ultrasound blood flow techniques and photoacoustic imaging, therefore, giving context to the research presented in the thesis. Chapter 3 introduces a new method for estimating blood perfusion and providing perfusion mapping validating it using simulations carried out on a powerful software called Field II. Chapter 4 validates the proposed method of estimating blood perfusion on experiments on phantoms and in-vivo by using a Visualsonics LZ250 21MHz linear array transducer as well as an ATL L7-4 linear ultrasound transducer

connected to a Verasonics Vantage programmable ultrasound system. Ultimately, Chapter 5 will conclude the work described in this thesis underlining applications and future work that can be accomplished.

Chapter 2

Background

2.1 Tissue Perfusion

Tissue perfusion is crucial for organ functions such as muscle contractions and exchange of oxygen and carbon dioxide. Sufficient tissue perfusion and oxygenation are of major importance in metabolic processes and influence tissue repairs and resistance to infectious organisms [45]. Furthermore, tissue perfusion should be evaluated on local tissue level and evaluation of this important physiological parameter is of fundamental significance for the outcome of medical treatments in patients diagnosed with cancer, for instance.

Moreover, tissue perfusion is extremely valuable in assessing organs for transplants and to monitor the function of organs in transplant recipients. However, most methods of evaluating perfusion in transplanted organs, such as scintigraphy, are expensive and use radiating substances.

Therefore, new non-invasive and non-radiating techniques for measuring tissue perfusion are needed and this research aims to bridge this gap.

2.2 Ultrasound Theory

The frequency range of audible sound goes from 20Hz to 20kHz. Any acoustic wave with frequency above 20kHz is considered an ultrasound wave. As any pressure wave, ultrasound waves need a medium to propagate. This propagation is mostly due to longitudinal motion (compression/expansion) in

most media including air, water, and tissue. The exception happens in non-gaseous media where ultrasound waves propagate in the form of shear wave (side-to-side motion).

The speed of ultrasound, c, depends on the properties of the medium and can be calculated as [51]:

$$c = \sqrt{\frac{1}{k\rho}} \quad (2.1)$$

Where k is the material compressibility and ρ is the density of the material. The denser the medium, the slower the speed of propagation.

The foundation of ultrasound imaging techniques lies on measuring reflected echoes after transmitting ultrasound waves in a medium. The concept of acoustic impedance is important in describing the propagation of ultrasound. The acoustic impedance Z is defined in Equation 2.2 [51].

$$Z = \rho c \quad (2.2)$$

The ultrasound wave is generated by an ultrasound transducer. Several transducers are currently available in the market, such as linear array transducers, phased-array transducers and convex transducers, which are used to image different body parts. To image the microvasculature, linear array transducers are generally used given the good near-field resolution. [48].

Ultrasound transducers are responsible for transmitting ultrasonic pulses and receiving the backscattered echo. Within each transducer there is a single element or an array of piezoelectric crystal elements. When a transient voltage is applied to a piezoelectric element, it vibrates at its resonant frequency (based on the width of the crystal) and generates an ultrasound pulse. Likewise, when piezoelectric crystals receive the backscattered echo sound waves, they produce an output voltage. Signals are detected by measuring the output voltage on a

subset of elements and by performing beamforming operations. All backscattered echoes from one transmitted pulse must be collected before transmitting the next pulse and the time-of-flight is proportional to the depth [49].

The transmitted echoes are backscattered due to reflection and scattering. Reflection is caused by an abrupt change in acoustic impedance and it provides information about the structural components of the tissue being imaged. The strength of the scattered signal and the variable intensity of the scattered signal with respect to angular direction (anisotropy) are determined by the physical properties of the scatterer [51].

Furthermore, for acoustic waves traveling in a medium, the pressure amplitude will decrease exponentially due to the continuous acoustic absorption and scattering as it collides with molecules, an effect known as attenuation. Attenuation is a non-linear and frequency dependent process. For soft tissue, attenuation can be estimated using Equation 2.3 [51].

$$\alpha = \alpha_0 f^n \quad (2.3)$$

Where α_0 is the temperature dependent factor, f is the central frequency of the transducer and n is defined by the material parameter that is between 1 and 2 for soft tissues. Due to attenuation the acoustic wave amplitude decay can be defined as shown in Equation 2.4 [51]. Where A_o is the original acoustic amplitude and z is the distance traveled by the wave in a medium. Ultrasound attenuation is also related to the frequency and higher frequencies will attenuate faster in tissues.

$$A(z) = A_0 e^{-\alpha(z)z} \quad (2.4)$$

When longitudinal waves travel from one isotropic medium to another with a smooth interface, the angle of incidence on the interface and the difference in acoustic impedance causes transmitted wave to both reflect and refract. The

material properties and the incident angle determine the angles of reflection and transmittance and their respective wave amplitudes. The relationship between angles of incidence, reflectance and transmission are governed by the law of reflection and Snell's Law, which can be expressed as $\theta_i = \theta_r$ and $\frac{\sin\theta_i}{sin\,\theta_t} = \frac{c_i}{c_t}$, where θ_i is the angle of incidence, θ_t is the angle of transmission, c_i is the speed of the sound in the incident medium and c_t is the speed of the sound in the transmitted medium.

Snell's Law also states the existence of a critical angle, which, in the case the angle of incidence is greater than the critical angle, the acoustic wave will be reflected completely with no energy loss. The critical angle, θ_{cr}, can be calculated as $\arcsin\left(\frac{c_i}{c_t}\right)$, $ci < ct$.

For an acoustic wave changing mediums the reflection and transmission coefficients of the pressure wave intensity can be expressed as [51]:

$$R = \frac{Z_t \cos\theta_i - Z_i \cos\theta_t}{Z_t \cos\theta_i + Z_i \cos\theta_t} \quad (2.5)$$

$$T = \frac{2Z_t \cos\theta_i}{Z_t \cos\theta_i + Z_i \cos\theta_t} \quad (2.6)$$

Where Z_i and Z_t are the acoustic impedance of the media for the incident and transmitted wave respectively.

2.3 Ultrasound Imaging

Ultrasound imaging has become a popular clinical imaging modality due to its low-cost, portability and non-invasiveness. Applications on ultrasound imaging go from imaging the eye to visualizing blood flow and destructing kidney stones [50].

In order to acquire appropriate images based on the different applications, one would have to choose a proper transmit pulse sequence. For instance, it is possible to focus ultrasound signals on a small focal region within the image by using curved arrays to increase signal-to-noise ratio (SNR). For linear arrays, multiple focal points can be transmitted at once to increase acquisition speed at the cost of resolution (decreased due to interference between multiple focal zones).

Furthermore, the use of ultrafast ultrasound imaging combined with specific reconstruction techniques made real time, non-invasive ultrasound applications for functional brain imaging and imagining of mechanical properties of tumors tangible [52].

In this section, two ultrasound imaging techniques will be explained: plane wave and focused ultrasound.

2.3.1 Plane Wave Imaging

Conventional medical ultrasound images are generally acquired sequentially one line at the time, which results in limited frame rate and an optimal focus at one depth. An alternative method is plane wave imaging. As the name suggests, plane wave imaging uses unfocused plane-wave transmissions. This technology, together with advancements in digital signal processing units, field programmable gate arrays (FPGAs) and graphical processing units (GPUs), allows imaging at frame rates higher than 1000 frames per second [54].

Nevertheless, for a single plane-wave transmission, lateral resolution and SNR are compromised due to lack of transmit focusing.

To overcome this limitation, it is possible to transmit several tilted ultrasound beams with different angles and the backscattered signals will be combined together to produce a full image. The angle compounding method

significantly improves image quality and enables blood flow imaging even though the frame rate improvement is partially sacrificed.

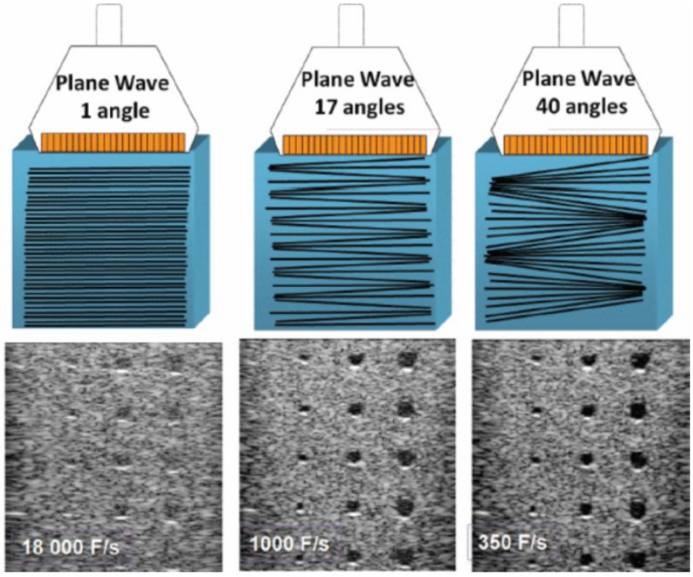

Figure 2.1 – Ultrafast ultrasound imaging sequences for a typical medical imaging setup by Tanter *et al.* [52], IEEE Transactions on Ultrasonics, Ferroelectrics and Frequency Control © 2014 IEEE.

Viti *et al.* [55] compared the use of compounded plane wave and focused wave transmission in detecting contrast agents. The conclusion was that compounded angle significantly improved contrast-to-noise (CNR) ratio as can be seen in Figure 2.1. Therefore, this method is going to be used throughout the research.

2.3.2 Focused Imaging

Traditional ultrasound systems used focused pulses meaning that they transmit and receive pulses one line at the time. However, this method has a limited frame rate, which is strongly related to penetration depth, due to the

time-of-flight of ultrasound and the necessity to acquire several scan lines (A-scans) to form a 2D B-scan image.

An ultrasound transducer transmits focused ultrasound beams in different lines of the image and use the reflected backscattered echoes to generate one A-scan line of a 2D B-scan image as seen on Figure 2.2.

The maximum frame rate that can be generated using focused ultrasound is as follows [51]:

$$FR_{focused} = \frac{c}{2d} \cdot \frac{1}{\#lines} \quad (2.7)$$

Where c the speed of ultrasound in tissue, d Is the distance from the ultrasound transducer and #lines is the number of lines for one whole frame.

The limitation of using focused ultrasound in estimating tissue perfusion is exactly due to its limited frame rate since highly effective clutter filters rely on large ensemble sizes that are not possible to achieve using focused ultrasound imaging.

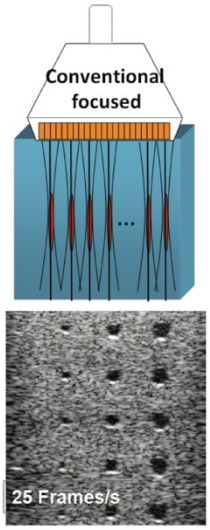

Figure 2.2 – Conventional focused ultrasound by Tanter *et al.* [52], IEEE Transactions on Ultrasonics, Ferroelectrics and Frequency Control © 2014 IEEE.

2.4 Ultrasound Perfusion Imaging

Ultrasound perfusion imaging has real time capabilities is relatively inexpensive, non-ionizing and non-invasive which gives it an advantage compared to other methods of imaging perfusion.

This section describes the theory behind contrast-enhanced ultrasound imaging (CEUS) and other US techniques capable of estimating tissue perfusion without the need of contrast enhancement.

2.4.1 Perfusion Imaging Using Contrast Agents

Microbubble contrast agents have magnitude ranging from 2μm to 6μm [1] and are filled with perfluorocarbon or another low-solubility gas. The microbubble is stabilized by a thin shell that can be either stiff or flexible and it is usually made of lipid, protein or polymer to enhance circulation in the bloodstream [1,2].

The basic idea is that microbubbles (MB) will increase the echogenicity of blood [2,3,4,5,6,7,8,9], but there are other relevant characteristics related to MB. For instance, microbubbles are designed to resonate at a frequency in the range used in US systems, therefore, the scattering cross-section does not depend only on the microbubble size, but it can increase dramatically at resonant frequency [1,9].

In addition, at high acoustic pressures near or at the resonant frequency, microbubbles behave as nonlinear scatterers producing a wide range of frequency components (harmonic frequencies) at the receiver [1,7,9,10]. These frequency components range from subharmonic ($f_0/2$) to ultra-harmonic frequencies ($n.f_0$)

[7,10], where f_0 is the transmitted frequency. By selecting the appropriate frequency components, it is possible to improve contrast detection by suppressing tissue signal [7]. One contrast specific imaging model widely used is called harmonic imaging (HI) or second harmonic mode [7,9,10]. In this respect the signal is received at the second harmonic (twice the fundamental), at which the magnitude of the signal backscattered from blood is greater than that of a tissue [9].

At even higher pressure the bubbles are disrupted, and a transient signal is emitted. This signal can be interpreted as a MB signature [1,8].

Essentially, there are two different approaches to estimate perfusion using US harmonic imaging techniques. The first one uses a continuous infusion of MB and low-frequency, high-pressure pulses to image. The second one is based on a bolus injection and low-power imaging [11,12]. This section will describe both techniques.

2.4.1.1 Microbubble Destruction/Replenishment Model

Wei *et al.* [13] was the first to analyze the replenishment kinetics following the destruction of a microbubble. He used the transient response effect to assess myocardial perfusion [5,8,9,12], and this process can be described as follows.

Figure 2.3(a) it is possible to notice that MB are injected with velocity v. When high-pressure pulses destroy microbubbles in a sample volume with width E (Figure 2.3(b)), the echo intensity would suddenly drop generating a “negative-bolus”. The intact MB will then reperfuse this volume at velocity v, and after some time T, microbubbles would fill the entire volume and the echo intensity would be restores to the original one (I_0). This process is monitored by acquiring a sequence of B-mode images to produce the wash-in time-intensity curve (TIC) [8,9,14].

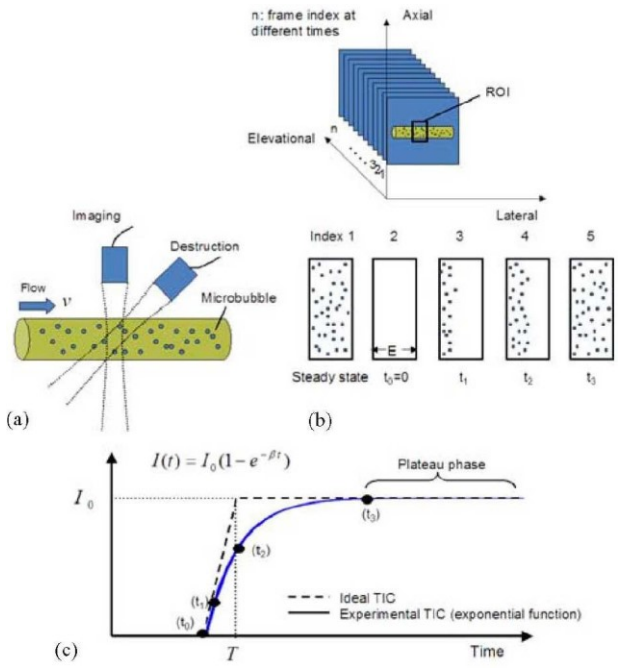

Figure 2.3 – Microbubble destruction/replenishment model. Captions and print from Microvascular flow estimation by contrast-assisted ultrasound B-scan and statistical parametric images by Tsui *et al.* [14], IEEE Transactions on Information Technology in Biomedicine © 2009 IEEE.

Ideally, the echo intensity should change as the dashed curve in Figure 2.3(c), however, the TIC behaves more curvilinear as shown by the solid line in Figure 2.3(c). Therefore, Wei *et al.* [13], proposed a mono-exponential function to model TIC, as can be seen in Equation 2.8 [8,9,14].

$$I = I_c + (I_0 + I_c)\left(1 - ce^{-\beta(t - t_0)}\right) \quad (2.8)$$

Where I_c is the clutter echo intensity, β is the constant related to the rate at which the echo intensity increases, and c describes the degree of destruction of MB, which also affects I_0 and β [8,14]. In the case where the clutter was completely removed, and microbubbles have been completely destroyed, Equation 2.8 can be simplified as [8,14]:

$$I = I_0(1 - e^{-\beta}) \quad (2.9)$$

By taking the first order derivative, the slope of the tangent of the TIC at the origin can be expressed as [14]:

$$s = I_0\beta \quad (2.10)$$

From Figure 2.3(c), we can notice that s is also equal to $\frac{I_0}{T}$, therefore [14]:

$$\beta = \frac{1}{T} \quad (2.11)$$

Consequently, the flow velocity can be calculated as [14]:

$$\upsilon = E\beta \quad (2.12)$$

Moreover, the flow rate f can be further expressed as the product between the cross-sectional area and the flow velocity. It is important to notice that β depends on T^{I_0}, but this is a hard parameter to measure due to the fluctuations of the TIC in the plateau phase, therefore, according to [14], β is calculated by:

$$\beta = \frac{-\ln(0.2)}{T_{80\%}} \quad (2.13)$$

Where $T_{80\%}$ represents the time to achieve 80% replenishment.

From the above description, it is clear that choosing proper region-of-interest (ROI) or volume (represented by the width E in the description above) is crucial for a good perfusion estimation. When the ROI is composed by perfused and non-perfused areas it is difficult to estimate the TIC since, at low frequency, clutter filter appear at 40-60 dB higher than blood flow and the 8-25 dB blood flow signal enhancement generated by MB is not enough to compensate for the clutter signal. Therefore, a clutter filter needs to be applied which can increase considerably the computational complexity. Furthermore, the use of high-pass filters can remove some flow information when signals associated with clutter and blood overlap [8,14].

At face of this, Tsui *et al.* [8] proposed the use of ultrasound images that are independent of the backscattering intensity to monitor microbubble replenishment. Therefore, a new imaging method based on the Nakagami statistical parameter was proposed to estimate the so-called time-Nakagami-parameter curve (TNC), which is analogous to the TIC. The Nakagami image allows only the visualization of scatterers concentration by analyzing the probability density function of the backscattered signal [8,14]. From there, the TNC curve was also fitted according to the monoexponential model.

This hypothesis was tested in phantom and in vivo. For the phantom experiment the TNC proved to be more robust than the TIC when tissue clutter was present, and it did not require additional wall-filter. However, the in vivo experiment showed that, if no wall-filter is used, the TNC cannot be used to estimate microcirculation flow. This happens because the excess of tissue affects TNC and TIC in a way that they do not behave exponentially [8]. Still, when a wall-filter was applied to both TNC and TIC, Tsui's method [8] outperformed Wei's [13] as can be seen in Figure 2.4, where it is possible to notice that the TIC designated a perfusion area as non-perfused as indicated by the white arrow.

Another issue that is raised by this technique is that US images can show artefacts created by motion related to patient's respiration or probe displacement. These artefacts affect the calculation of perfusion parameters, and therefore must be removed from the interested ROI [15]. According to [2], Pollard *et al.* [100], combined destruction -reperfusion imaging with real-time motion correction to make the technique more robust in case of tissue motion.

Moreover, Rognin *et al.* [16] developed an automatic motion compensation strategy based on multi-mask which tried to assure the reliability of perfusion parameters as can be seen in Figure 1 from [16] . It is possible to notice that the low frequency component was removed which allowed a better fit of the signal by a mono-exponential model.

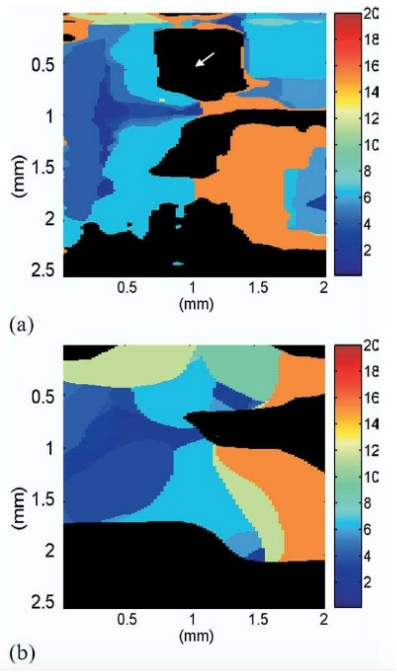

Figure 2.4 – Flow velocity parametric images of rabbit eye by using (a) conventional B-mode image and (b) Nakagami image. Captions and print from Microvasculature flow estimation by microbubble-assisted Nakagami imaging by Tsui *et al.* [8], Ultrasound in medicine & biology (2009).

However, these methods assume that the motion is always on the acquisition plane, which is not necessarily true for in vivo experiments.

Therefore, Mulé *et al.* [15], proposed a method that selects the frames acquired at the same respiratory cycle by using Principal Component Analysis (PCA). This is based on the assumption that not only one, but several components held information about the respiratory cycle. In addition, some information about the respiratory frequency need to be known a priori to estimate respiratory motion, and therefore generate the two subsequences. The preliminary results of this study were promising.

The destruction/replenishment model has proven to be a reliable technique for obtaining semi-quantitative parameters related to tissue perfusion, and it also provides information about the morphology of microcirculation. Nevertheless, there is still room for improvement mainly on fields such as motion compensation, and finding better fits for the time-intensity curve in situations where it does not obey the exponential model.

2.4.1.2 Microbubble Non-Destructive Model

With the development of contrast-specific imaging strategies such as Vascular Recognition Imaging, which combines Doppler information with phase analysis [1], and Cadence Contrast Pulse Sequencing, which interrogates each image line with pulses with different amplitudes and phases [1,2], it was possible to detect microbubbles non-destructively at high contrast-to-tissue ratios [2].

As mentioned before, the second harmonic imaging (HI) is widely spread and commercially available combined with the contrast-specific imaging strategy called pulse inversion [10]. In this case, a pulse pair 180 degrees out of phase from one another is transmitted and the received signals are superimposed in order to cancel odd harmonics [3,10].

Nonetheless, nowadays, it is well known that there is second harmonics generation and accumulation in surrounding tissues, culminating with reduced blood-to-tissue contrast. A solution for this problem is to receive at subharmonic frequencies ($\frac{f_0}{2}$) at which it is possible to achieve near complete tissue suppression since there is no generation of subharmonics in surrounding tissues [7,10].

Therefore, it is possible to track the bolus of microbubbles in order to generate time-intensity curve to follow the wash-in and wash-out of MB [1]. This

time-intensity curve is also fitted following the monoexponential model as described on the previous section.

For both, destruction/replenishment and bolus kinetics analysis, ideally the raw radiofrequency (RF) signal should be used for curve-fitting [17]. However, RF data is not always made available by ultrasound manufacturers, therefore, the log-compressed signal needs to be converted before curve-fitting. This can generate errors in perfusion parameter estimation unless two conditions are respected: a) the gain settings of the system should be adjusted to prevent saturation and b) sufficiently high dynamic range log-compression (>45dB) should be used [17] so the signals from blood flow and tissue can be well distinguished [15].

2.4.1.3 Applications

Contrast-enhanced ultrasound imaging (CEUS) is approved in the United States for enhancing heart structures such as the ventricular chamber. Furthermore, it has been used off-label in applications suchlike breast, liver and kidney imaging [2].

Bruce *et al.* [3] used microbubbles contrast agents at a low mechanical index (MI), which avoids microbubbles destruction, to acquire flow information in large and small vessels simultaneously. By using harmonic imaging combined with pulse inversion acquisition the group discriminated perfusion and vascular flow based on parallel processing of signals and considering that, for microbubbles moving at higher speeds, the Doppler shift can be easily detected. This technique was able to produce a signal-to-clutter ratio as good as -4dB and provides additional perfusion information when compared with color Doppler. Figure 2.5 illustrates the parallel signal paths. The top path illustrates conventional pulse inversion processing for perfusion while the other two

illustrate the detection of fundamental and harmonic signals for higher velocity MB circulating in larger vessels.

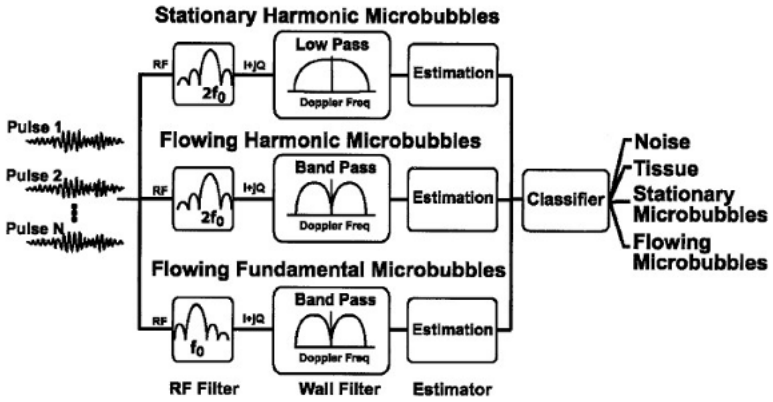

Figure 2.5– Illustration of parallel processing for simultaneous detection of perfusion and vascular flow using contrast-agents. Captions and print from Vascular flow and perfusion imaging with ultrasound contrast agents by Bruce *et al* [3] Ultrasound in medicine & biology (2004).

Nonetheless, this method still relies on MB moving at considerable higher speed which is not suitable to estimating perfusion in the microvasculature, a gap this research aims to fill.

Perfusion imaging using contrast agents has also been used to provide information about tumor perfusion and morphology simultaneously [4]. Hoyt *et al*. [4] analyzed how breast tumors in six female patients responded to treatment. The results were promising. The high-contrast perfusion profile due to angiogenesis made possible the analysis of tumor morphology, while the time-intensity curve changed over time as the tumor responded to drug treatment, as expected.

Chomas *et al*. [5] also monitored tumor therapy by using CEUS in subharmonic imaging (SHI) setup. Experiments in vitro suggest that this method

is able to estimate flow velocities in the range of 0.1mm/s and 1cm/s. The contrast-agent-to-tissue ratio was as good as 23dB, and the results were compared with contrast-assisted CT and histology as shown in Figure 2.6.

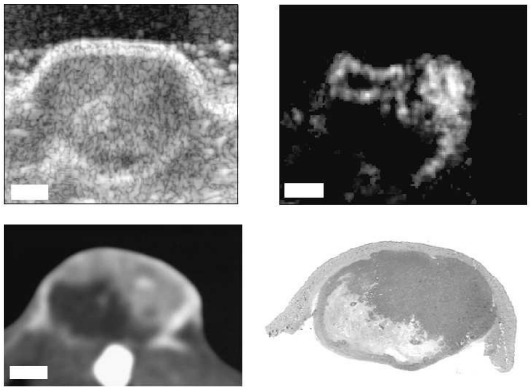

Figure 2.6 – Comparison of contrast-enhanced US, histological staining, and contrast enhanced CT of a rat breast tumor. (a) B-mode US (b) Contrast-enhanced US (c) Contrast-enhanced CT (d) Histology staining. Captions and print from Subharmonic phase-inversion for tumor perfusion estimation by Chomas *et al.* [5], IEEE Ultrasonics Symposium © 2001 IEEE.

Perfused regions in the tumor correlated with histology findings, but this method provides a better spatial resolution when compared with CT, and it provides additional information about perfusion parameters when compared with histology [2].

Furthermore, CEUS is a promising technique for detection of molecular response. Targeted contrast agents have been developed by linking specific ligands to microbubbles shells therefore favoring adhesion to specific markers of disease progression [18]. Korpanty *et al.* [18] targeted microbubbles to evaluate the efficacy of anti-angiogenic therapy of pancreatic tumor in animal models. The results showed significant enhancement in tumor perfusion when targeted MB were used instead of non-targeted ones.

Hence, studies have demonstrated the potential of CEUS in several applications such as the prediction of anti-angiogenic therapy response, liver lesion detection and characterization, and stroke management [2,18]. This is extremely important because it shows the advantage of ultrasound imaging compared with other perfusion imaging modalities.

However, perfusion parameters measured through CEUS are not well-established clinical tools yet and the use of contrast-agents is a concern in several applications and therefore its real life medical significance is still limited evidencing the importance of a method for estimating tissue perfusion free of contrast-agents such as the one proposed in this study.

2.4.2 Perfusion Imaging Without Contrast Enhancement

Microbubbles can be metabolized by humans. The gas content is exhaled by the lungs and shell components re-metabolized by the liver or filtered by the kidney. Adverse human reactions are rare, but low blood pressure has been observed after MB injections, and some deaths have been reported in cardiac patients [1]. For this reason, microbubbles are not approved by the Food and Drug Association (FDA) for use in many applications. Therefore, the capability of estimating tissue perfusion without the need of contrast enhancement has gaining more focus.

One technique used to display the scattered ultrasound power from moving blood in tissue is ultrasonic Power Doppler (PD) imaging, which is highly sensitive to slow disorganized movements of red-blood-cells (RBC) [9,19,20,21]. PD does not provide any information about the rate of flow of blood and is insensitive to blood speed and direction. It is also extremely vulnerable to tissue

clutter and acquisition noise [21]. Therefore, the one main challenge of this technique is to increase signal-to-noise + clutter ratio (SNCR) [20]. This can be done by suppressing noise and clutter components [20,21], and by using high-frequency US systems since at higher frequencies the echogenicity of blood is significantly higher than at low diagnostic frequency.

Extensive work has been done over the years in order to suppress clutter signal originated from stationary and slowly moving tissue. Several clutter filters have failed their purpose due to the assumption that tissue and blood flow signals have completely different spectrums, which is not true in cases where blood flow has the same magnitude as tissue motion [22].

Based on this assumption, US data was usually filtered based exclusively on the temporal dimension using finite impulse response (FIR) or infinite impulse response (IIR) filters [20,21,23,56]. However, tissue and blood flow also present different spatial characteristics since tissue movement towards the transducer can be seen as a shift in the RF data while RBC movement changes the profile of the RF data [22]. Therefore, it is now well accepted that Fourier filters do not provide the best result for separating tissue from slow blood flow signal [20,21]. As an option, it is possible to extend the filter dimension to use information from both spatial and temporal domains to isolate blood signal. Eigenfilters, specifically singular-value decomposition (SVD) filters, decompose this multidimensional data using eigenvectors or singular vectors of the correlation matrix or Casorati matrix [20], which contains all statistical information [20,21,23,22]. The eigenvectors or singular vectors are orthogonal and statistically independent from each other whereas the normalized eigenvalues or singular values represent the amount of variance contributed by each eigenmode or singular mode. Since tissue is more echogenic than blood, and both contribute more to the variance than noise, it is possible to assume that the first few eigenvalues will be dominated by tissue clutter, followed by blood eigenvalues and then noise. Therefore, isolating the blood subspace is possible by identifying

the clutter-blood and blood-noise interfaces and suppressing the eigenvalues or singular values outside this range [20,21].

The theory behind SVD filters is as follows:

Data from ultrasound acquisition can be organized as a spatiotemporal matrix of the form *s(x,z,t)*. This 3D matrix has dimensions (n_x , n_z , n_t), where n_x is the number of spatial samples on the x-direction, n_z is the number of spatial samples on the z-direction, and n_t is the number of time samples. The matrix is then reshaped into a 2D matrix, with one spatial domain and dimensions ($n_x x\, n_z$, n_t), called the Casorati matrix **S** [22, 23].

The singular value decomposition of the Casorati matrix relies on finding three matrices such as [22]:

$$\mathbf{S} = \mathbf{U}\Delta\mathbf{V}^{*} \quad (2.14)$$

Where Δ is a non-square (n_x x n_z, n_t) diagonal matrix, **U** and **V** are orthonormal matrices of dimensions ($n_x x\, n_z$, $n_x x\, n_z$) and (n_t , n_t) respectively, and "*" stands for conjugate transpose. The columns of **U** and **V** represent the spatial and temporal eigenvectors respectively. Moreover, U is also the eigenvector of the covariance matrix $\mathbf{SS}^{*}$ and V is the eigenvector of the covariance matrix $\mathbf{S}^{*}\mathbf{S}$ [22].

Matrix **S** can be considered a sum of separable matrices $\mathbf{A_i}$, that in turn can be written as the outer product of two vectors $\mathbf{A_i} = U_i \otimes V_i$. Therefore, **S** can be decomposed as [22]:

$$S = \sum_i \lambda_i A_i \; = \sum_i \lambda_i U_i \otimes V_i \quad (2.15)$$

U_i and V_i are the i^{th} columns the orthonormal matrices **U** and **V** and λ_i are the ordered singular values. U_i corresponds to the spatial signal with length n_t and V_i corresponds to the temporal signal also with length n_t. Each vector U_i describes

the 2D image I_i with dimensions (n_x, n_z) and modulated by V_i, and **S** comprises on the addition of all I_i images. As previously explained the blood signal can be isolated by identifying the clutter-blood and blood-noise interfaces and the blood signal is calculated using Equation 2.16 [22].

$$\boldsymbol{S^f = U\Delta^f V^*} \quad (2.16).$$

Where $\mathbf{S^f}$ is the filtered data (blood signal), and $\mathbf{\Delta^f}$ is the diagonal matrix of singular values suppressing tissue and noise signals. Figure 2. illustrates how the ultrasound data is reorganized so singular value decomposition can be performed.

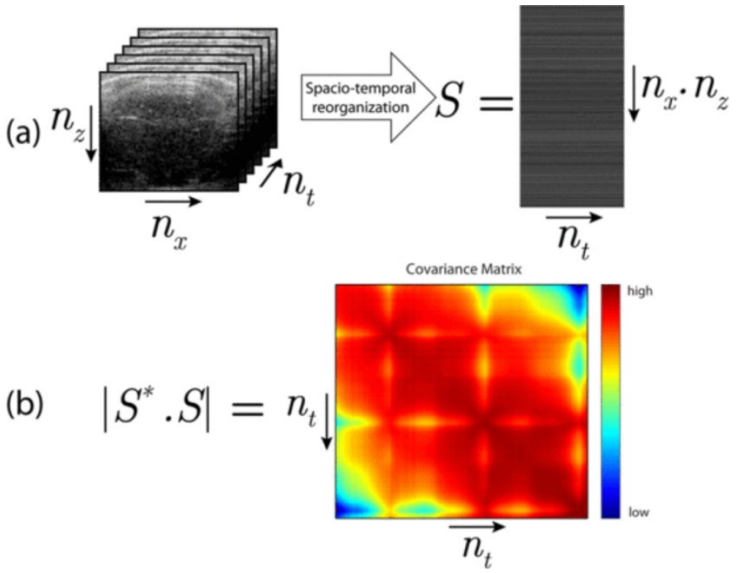

Figure 2.7- (a) The ultrafast Doppler acquisiton forms a 3D stack of images with 2 spatial dimensions and one temporal dimension. It is reshaped in one spatiotemporal representation (Casorati matrix) where all pixels at one time point are arranged in one column. As a consequence all time points for one pixel are arranged in one row. (b) The covariance matrix is presented here in magnitude and is of dimension n_t x n_t. Captions and print from Spatiotemporal clutter filtering of ultrafast ultrasound data highly increases Doppler and fUltrasound sensitivity by Demene *et al.* [22]. IEEE transactions of medical imaging © 2015 IEEE .

Additionally, researchers started to use ultrafast ultrasound imaging based on unfocused wave transmissions to acquire wide fields of view (FOV) at a very high frame rate. The use of this method came with a loss in focusing capabilities, even when a set of tilted plane waves was used to increase resolution. However, the use of SVD on those large datasets improved Doppler sensitivity considerably [24,22]. This is because large Doppler ensemble sizes (>100) were possible due to whole frame acquisitions per transmit, unlike in scanline imaging, where scanline ensemble sizes (the number of repeated ultrasonic emissions along a line of sight) were limited to around 10. The longer Doppler ensembles associated with unfocused wave transmissions resulted in greater sensitivity to slow blood flows.

Demene *et al.* [22] analyzed the performance of the SVD filter in different applications and compared it with temporal filters. They concluded that the SVD filter removes strong motion artifacts occurring during freehand exams and improve the detection of small vessels characterized by low flow speeds even if tissue motion is present. The group showed the impact of SVD filtering in clinical applications such as kidney, liver and thyroid imaging. Figure 2.8 shows PD images illustrating how the SVD filter outperforms Butterworth filters for imaging a transplanted kidney. They also imaged neonate brains which was interesting since it was not possible to ask patients to hold their breath, and therefore motion was unavoidable.

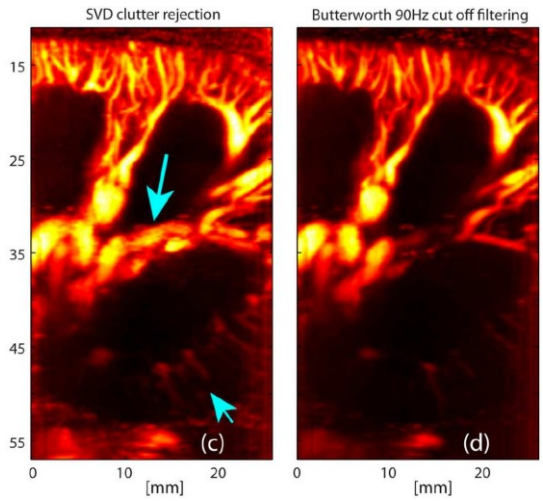

Figure 2.8- PD images comparing between SVD and IIR filter shows how SVD outperforms the later in imaging low flow speed. Captions and print from Spatiotemporal clutter filtering of ultrafast ultrasound data highly increases Doppler and fUltrasound sensitivity by Demene *et al*. [22], IEEE transactions of medical imaging © 2015 IEEE.

The SVD filter proposed by Demene was applied in the entire three-dimensional data set (2D of space plus time) assuming that the noise in the whole image is independent and identically distributed (i.i.d). This assumption may be valid for functional ultrasound brain imaging in mice where the imaging FOV is small and shallow. However, for *in vivo* human imaging the nature of noise varies spatially within the FOV due to depth-dependent attenuation [23].

Thus, Song *et al*. [23] proposed a new block-wise local SVD clutter filter technique (for ultrafast plane wave imaging) that operates in local data blocks where the local noise distribution is approximately i.i.d [23]. Furthermore, it addressed a limitation presented in Demene's study where no adaptive method for the choice of the threshold used for singular vector rejection was proposed. In Song's study the singular value cutoff thresholds for tissue-blood and blood-noise separation were adaptively determined based on the local signal and noise characteristics.

This new method provided an increase of more than two-fold in SNR and more than three-fold in contrast-to-noise (CNR) ratio when compared with existing SVD-based clutter filtering methods. More detailed vasculature could be resolved and a significant amount of background noise was suppressed by using this method. The spatial resolution of small vessels which is mostly determined by the ultrasound imaging resolution (e.g. frequency, pulse length, etc.) was not compromised by this method since no spatial averaging was performed within each processing block. Furthermore, the use of adaptive methods to choose block-wise SVD filter thresholds made it more robust in processing data acquired from different organs with different tissue and blood signal characteristics [23]. Figure 2.8 shows PD images to compare global and local SVD filters. This illustrates how the later outperforms the first.

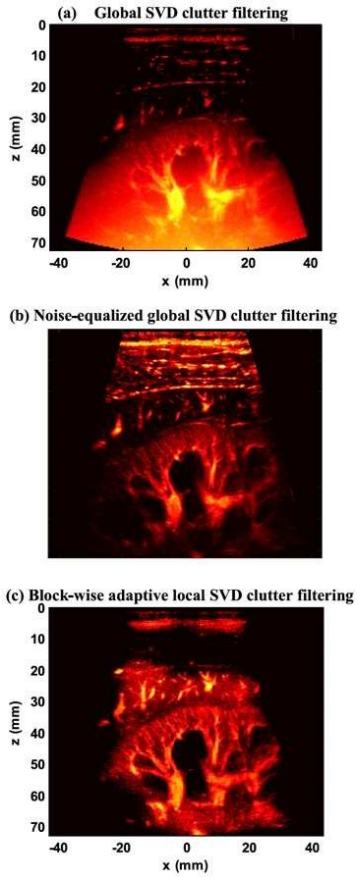

Figure 2.9 – (a) Clutter filtering using global SVD filtering approach (b) clutter filtering after noise equalization (c) Clutter filtering on the same dataset using block-wise adaptive local SVD filter. Captions and print from Ultrasound small vessel imaging with block-wise adaptive local clutter filtering by Song *et.al* [23], IEEE transactions on medical imaging © 2017 IEEE.

The limitations of the block-wise SVD filter as well as Eigenfilters in general uses high computational cost compared to conventional high-pass clutter filters. Moreover, the user needs to adjust the block size according to the ensemble length to achieve optimal performance and no adaptive method was proposed to facilitate this choice. In addition, this method still models the noise as Gaussian which may not be the best noise model to simulate spatially varying complex noise seen *in vivo* [23].

The exponential evolution of computational power of GPU based electronics changed ultrasonic imaging. Therefore, Kim *et al.* [20] was able to propose the use of SVD filter for scanline pulse-echo PD imaging instead of ultrafast plane imaging. This substantially improved SNCR and Doppler Frequency resolution enabling the visualization of slow perfusion that was not visible using other PD techniques.

The acquired data array has initially two spatial dimensions (axial and lateral) and two temporal dimensions (slow-time and frame-time). Temporal sampling was adjusted to increase the density of independent samples in the low-frequency Doppler spectrum where perfusion signals dominate. This 4D data was then reorganized by combining the two spatial components into one, resulting in a 3D data array [20].

In order to overcome the issue of SVD filters suppressing perfusion signal when operating on slow-time echo signals, Kim *et al.* [21] proposed an extension of the SVD filter to work on this new 3D dataset. The increased dimension of the clutter filter was then called higher order SVD (HOSVD) technique and facilitated the isolation of signals coming from slow tissue motion and spatially disorganized RBC movement [20].

The construction of the HOSVD filter is based on the analysis of three basis vectors (one for each dimension), instead of two, which effectively separate signal components and enhance perfusion sensitivity in PD imaging. This technique was tested *in vivo* by analyzing muscle-perfusion of healthy and ischemic mouse limbs using a high-frequency ultrasound system [20].

Figure 2.10 shows PD images overlaid on B-mode US images to compare HOSVD and conventional temporal filters. The images show the signal power that describes relative flow and perfusion patterns. The extra data dimension analyzed by HOSVD allowed an increasing perfusion sensitivity through a longer

acquisition period (more than 1s) without discarding fast blood flow signals (as illustrated in Figure 2.10) [20].

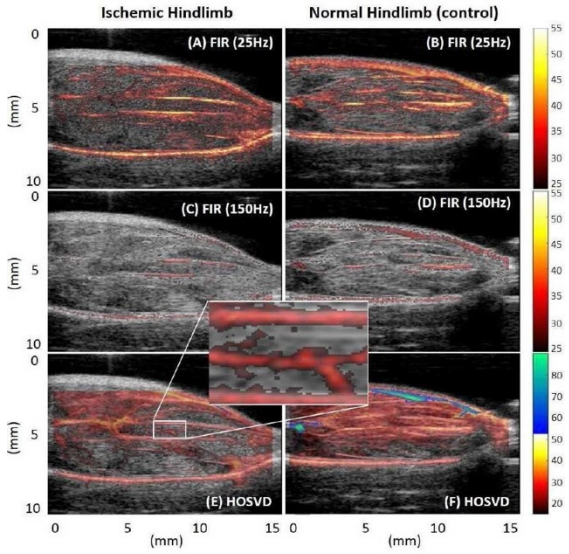

Figure 2.10 – PD images compared by using FIR filter and HOSVD applied to the same dataset. Captions and print from Expanding dimensions for improved perfusion sensitivity by Kim *et al.* [20] IEEE transactions on ultrasonics, ferroelectrics, and frequency control © 2017 IEEE.

The challenge for users is to define the proper subspace to isolate blood perfusion signals. Thus, the same research group proposed a statistical classifier that is applied at each of the three dimensions (slow-time, spatial and frame-time) in order to identify a proper blood subspace. This is done by analyzing five features estimated from the decomposition of eigenvalues and eigenvectors. Three of the features are related to the eigenvalue energy and two are similarity measurements. The results showed that blood and clutter power were well separated by using this method for the case of a narrow clutter bandwidth [21]. However, blood and clutter signals overlap when the bandwidth of the later increases as tissue moves with high amplitude. Moreover, the transducer was placed into a fixture and therefore free from hand motion which is unusual in clinical ultrasound.

The methods previously described to analyze tissue perfusion without contrast agents provide information mostly about the morphology of the microvasculature. PD imaging is highly sensitive to disorganized movements of RBCs, and it displays the signal power rather than the more physiologically relevant parameter, the blood flow itself. Therefore, those methods still lack the capability of providing quantitative perfusion measurements as it is possible to get from analyzing time-intensity curves generated by microbubbles.

Choi *et al.* [59] demonstrated a method to image the perfusion rates in superficial tissues using a combination of ultrasound and photoacoustic imaging systems. That study addressed the limitation of the power Doppler imaging mode in estimating flow change on capillary beds when tissue was compressed and then released, a scenario where flow signals from vessels are overwhelmed by tissue motion. Therefore, a new method relying on changes in PA signals during compression and release was proposed. A first-order negative exponential model was fit to PA signals and used to quantify perfusion rates. Ultrasound signals were used to track tissue motion adaptively using a strain estimation algorithm called AM2D [62].

The AM2D algorithm uses the RF signal to estimate the axial and lateral displacements of the tissues creating a deformation map. We found value in using the same algorithm during our *in vivo* experiments where subjects' movements are inevitable, and the failure of tracking tissue motion would affect the capability of the method proposed here to quantify tissue perfusion.

Although Choi's perfusion-rate estimation method [59] is a great advancement towards quantitatively estimating tissue perfusion it does not provide information on the morphology of the microvasculature since the photoacoustic signals from capillaries are spatially unresolvable.

Hence, there is still a need for a method that is able to provide those quantitative measurements without contrast enhancement combined with

information about the morphology of the microvasculature. We hypothesize that speckle tracking methods are able to provide important quantitative metrics. Those methods were first proposed to overcome the limitations of conventional Doppler ultrasound where only motions in the axial direction could be identified [25].

Echo signals backscattered from blood and tissue can be tracked since they behave in a pattern that remains relatively constant as blood or tissue moves. The speckle tracking can be done in one, two or three dimensions, depending on the dimensions of the ultrasound data available and the analysis of it leads to blood flow estimation [25]. Even though multidimensional speckle tracking is known to be computational expensive this is becoming less of a problem with advances in processing power.

In this study we provide perfusion mapping images and quantitative measurements of tissue perfusion by combining data acquired using speckle tracking methods, advances in clutter filtering and tissue motion compensation.

2.5 Photoacoustic Effect and Photoacoustic Imaging

Photoacoustic imaging systems rely on two main components: a source of energy and an acoustic detector [60]. The acoustic detector is usually an ultrasound transducer while the source of energy can be a pulsed nanosecond laser [47, 60] or microwave and radio-frequency (RF) waves [47]. Due to its long wavelength, RF waves cannot provide a good spatial resolution, while with short pulse lasers, it is possible to provide images with high resolution in larger volumes of tissue [47].

The photoacoustic effect and the process of acquiring photoacoustic signal happens as follows: when the tissue absorbs an EM pulse, the optical energy of

the signal is also absorbed. This generates a thermoelastic expansion producing acoustic waves [60]. Those acoustic waves reach the tissue surface at different times, and the ultrasound transducer is responsible to measure such waves, which will be used to generate the acoustic source distribution to mapping absorption properties [47]. Spatial resolution and the penetration depth can be adjusted based on the central frequency and the bandwidth of the ultrasound transducer [47,60].

To deliver EM pulses to the tissue it relies on optical fibers and mirrors. Moreover, the whole system should be connected to a microprocessor responsible for data acquisition, imaging reconstruction and image display [60].

The images are formed based on different optical absorption coefficients of tissues, and the magnitude of the photoacoustic (PA) signal depends on several factors such as the physiological condition of the tissue and the excitation beam wavelength (when the laser is the source of energy) [60].

To image the microvasculature, it is possible to use lasers with wavelength in the visible and near infrared spectrum where the main endogenous contrast is hemoglobin [43, 44, 47]. In addition, the image is practically speckle free, due to the low concentration of hemoglobin in tissue.

Based on the penetration depth in units of the transport mean free path (TMFP), there are three different types of photoacoustic imaging (PAI): quasi-ballistic, quasidiffusive and diffusive. The first is used for depths smaller than 1 TMFP, the second for depths between 1 and 10 TMFP, and the latter for depths larger than 10 TMFP [60].

In the quasiballistic regime the main implementation of the photoacoustic system is the optical-resolution photoacoustic microscopy (OR-PAM). Theoretically, the ballistic regime would measure only unscattered photons, but, to increase the signal, “scattered quasiballistic photons are also measured” [60]. The OR-PAM system consists of an objective lens used to tightly focus the laser beam into the tissue, and even though the ultrasound transducer is also focused, the optical focus is tighter than the acoustic one [43]. Therefore, the lateral

resolution is defined by the optical system, while the axial resolution is determined by the bandwidth of the transducer [60]. The OR-PAM can provide a high spatial resolution of 1-2μm [43].

The acoustic-resolution photoacoustic microscopy (AR-PAM) is the main implementation in the quasidiffusive regime. When using a high frequency ultrasound transducer the spatial resolution is around 50μm [43]. The system consists of conical lens used to widely focus the laser beam, and, as doing so, the acoustic focus gets tighter than the optical focus. As in the OR-PAM, the axial resolution is defined by the bandwidth of the transducer, while the lateral resolution depends on the numerical aperture (NA) of the lens and central frequency of the ultrasound transducer [60].

In the diffusive regime the main implementation is the photoacoustic computed tomography (PACT), where a diffusor is used to expand the beam and illuminate a larger region of the tissue while a transducer array is used to detect the PA waves all at once. Low frequency ultrasound transducers are used to increase penetration depth at the cost of spatial resolution.

2.5.1 Estimation of sO_2 from PA Signals

Estimating blood oxygen saturation (sO2) provides important information about the vasculature in the macro and micro level [57]. For instance, oxygen saturation is an important factor on the process of healing burns and wounds [32, 57, 58], and for the analysis of brain activities in small animals [32]. Moreover, abnormal oxygenation levels are related to the advent of ocular diseases such as cataract and glaucoma [59].

Furthermore, estimating blood oxygen saturation is critical in cancer research [25,32,57,58]. It is known that cancer microenvironments present abnormal levels of protein, oxygenation and PH values, besides of being associated with angiogenesis and metastasis [58]. Also, tumour hypoxia has a

close relationship with the resistance to chemotherapy and radiotherapy [25, 32, 57, 58]. Therefore, oxygenation measurements can help choosing the best treatment for different kinds of cancerous lesions.

Currently there are several techniques used to measure blood oxygen saturation. The traditional method is by using diffuse optical spectroscopy (DOS) [25,32, 57]. However, due to low spatial resolution (caused by optical scattering), oxygenation measurements need to be averaged over the volume of the biological tissue [32]. Another widely used technique is pulse oximetry, which is based on near infrared spectroscopy (NIRS), also lacking spatial resolution [25, 57].

Functional magnetic resonance imaging (fMRI) monitoring blood oxygen level dependent (BOLD) contrast can be used to quantify sO2 with high spatial resolution [25,29,30,57]. However, BOLD MRI is only sensitive to deoxyhemoglobin (HbR) and it cannot distinguish between change in blood oxygenation and perfusion [29, 30]. Other techniques such as positron emission tomography (PET) [25, 29, 30, 57], electron paramagnetic resonance imaging (EPRI) and single photon emission computed tomography (SPECT) can also quantify blood oxygen saturation [57]. Nevertheless, every technique described so far has disadvantages, the most common one being the need of exogenous contrast agents to provide functional information [57].

As explained in section 2.5 photoacoustic (PA) imaging is based on the detection of acoustic waves generated by thermal expansion when optical energy is absorbed by a sample [25, 29, 30, 32, 57, 58]. The pressure generated is proportional to the optical absorption coefficient of the tissue, therefore, multiwavelength measurements of PA signals can lead to information about the optical spectrum [32,57]. Since blood is rich in oxy- (HbO2) and deoxyhemoglobin, which are the strongest chromophores in the 650-900nm wavelength range, PA imaging can provide structural images of blood vessels [32]. Moreover, considering that blood absorption is determined only by HbO2 and HbR, multiwavelength PA measurements can be used to determine sO2 [32],

which is defined by the ratio of oxyhemoglobin concentration ([HbO2]) to total hemoglobin concentration ([HbO2]+[HbR]) [57].

Furthermore, using the estimation of sO2 one can also estimate the rate of oxygen consumption (MRO2), which is important for studying tissue metabolism and diseases related to oxygen metabolism such as diabetes [29, 30]. In a single vessel, oxygen flux can be estimated based on three parameters: cross-section area of vessel, sO2, and mean flow speed [30].

While photoacoustic Doppler flowmetry can be used to estimate flow speed, until now, accurate measurements can only be done for shallow depths [29,30]. Therefore, the use of ultrasound-based techniques as proposed in this study would be more appropriate to estimate flow speed deeper in the tissue. The use of Doppler ultrasound combined with photoacoustic has proven to provide a good estimation of MRO2 both in phantom and *in vivo* [29, 30]. However, measuring flow speed using Doppler ultrasound which is based on the phase shift of the received signal, is not accurate when the Doppler angle approaches 90 degrees [29, 30]. Thus, the autocorrelation method proposed in this study will be used to measure blood flow based on movement of scatterers inside the vessel, rather than based on the phase shift of the received signal. This approach uses a linear array high-frequency ultrasound transducer, instead of a single element ultrasound transducer, which has been used before.

In addition, it is known that tissue scattering is more echogenic than blood scattering [20,30], so we used a clutter filter. For the purpose of estimating blood oxygen saturation, we used a block-wise SVD filter. Since the tissue scattering and blood scattering contribute more to the variation of the signal than noise, and tissue is more echogenic than blood, we used the block-wise SVD to suppress all the eigenvalues outside the blood subspace. From the correlation matrices we calculate the temporal and spatial eigenvectors, which will be used to estimate the blood signal matrix as explained on Section 2.4.2.

The cross-section area of a single vessel can be quantified using the power Doppler technique on the filtered data [30]. This technique shows the strength of

scattering movement due to blood flow and the intensity of the power Doppler image is proportional to the number of scatterers moving within the vessel volume.

Throughout the years different approaches were proposed to estimate blood oxygen saturation from PA signals. For instance, Esenaliev *et al.* [99] proposed the use of exponential rise in PA signals [32, 57]. This approach is self-calibrating since it does not deal with absolute values of the PA signal, but rather its relative change. Therefore, the use of this method on PA signals acquired at different wavelengths lead to accurate values of sO2, independently of the surrounding tissue [57]. Nonetheless, this approach can only be used in vitro since it requires vessels with a predictable shape, such as planar boundaries, which is not feasible for in vivo applications [57].

Thus, in order to estimate sO2 in vivo, it is possible to analyse the peak amplitude of PA signals. The amplitude of a PA signal depends on three physical quantities: optical fluence, optical absorption coefficient, and the Gruneisen parameter [32, 57]. The local value of the optical absorption coefficient is based on the concentration of optical chromophores [32]. However, the relationship between chromophore concentration and optical fluence is not straightforward since optical fluence depends on the distribution of chromophores and scatteres in the whole region exposed to optical energy [32, 57].

Therefore, due to the unknown spatial distribution of fluence, estimating blood oxygen saturation becomes a hard task to accomplish using multiwavelength PA signals [32]. Knowing the photoacoustic signals at the surface $p(x,\lambda_k)$ and extinction coefficients $\varepsilon_{HbO2}(\lambda_k)$ and $\varepsilon_{Hb}(\lambda_k)$ one can solve the inverse problem of calculating the concentrations of oxy-and deoxyhemoglobin using the following Equation 2.17 [30].

$$\begin{bmatrix} p(x,\lambda_1) \\ \vdots \\ p(x,\lambda_n) \end{bmatrix} = \Gamma(x) \begin{bmatrix} \Phi(x,\lambda_1)\varepsilon_{Hb}(\lambda_1) & \Phi(x,\lambda_1)\varepsilon_{HbO2}(\lambda_1) \\ \vdots & \vdots \\ \Phi(x,\lambda_n)\varepsilon_{Hb}(\lambda_n) & \Phi(x,\lambda_n)\varepsilon_{HbO2}(\lambda_n) \end{bmatrix} \begin{bmatrix} C_{Hb}(x) \\ C_{HbO2}(x) \end{bmatrix} \quad (2.17)$$

Where the term Γ(x) represents both the relative Gruneisen parameter and the relative sensitivity, being wavelength independent. Therefore, not impacting the sO2 [30]. However, the wavelength dependent fluence $\Phi(x,\lambda_k)$ cannot always be neglected [29].

Under the assumption that the excitation wavelengths are considerably close, one can drop the wavelength dependent scattering, and therefore consider the optical fluence constant, assuming that the PA signal is proportional only to the local absorption coefficient [59]. In that case, solving the system of equations based on Equation 2.17 would lead to estimating sO2 [30].

$$\mu_a(\lambda_i) = \varepsilon_{Hb}(\lambda_i)[Hb] + \varepsilon_{HbO2}(\lambda_i)[HbO_2] \quad (2.18)$$

The number of equations in the system depends on the number of excitation wavelengths used to generate PA signals. Moreover, the same assumption can be used if the laser wavelength corresponds to the transparency window (650nm-1300nnm) [32]. Nevertheless, the absorption by blood at these wavelengths are low, which can lead to errors [32].

The problem of choosing the optimal wavelength for estimating sO2 have been addressed by several studies, but it depends on the application and may vary for different investigation depths. Furthermore, in most of these studies, the optical fluence is considered known from the scattering and absorption coefficient of tissues, which are usually treated as homogeneous. However, most of these methods require sophisticated models for absorption and optical transportation, which is an issue for real-time imaging [25]. In addition, heterogeneity of tissue prevents modeling fluence with sufficient accuracy [32].

Therefore, in this study sO2 will be estimated using the system of equations based on Equation 2.15, which, indeed, has limitations, but has proven to provide a good estimation of blood oxygen saturation [29,30,58,59].

Chapter 3

Simulations

3.1 Introduction

Simulations are an inexpensive and safe way to experiment with system models while providing a deeper understanding about the system. Moreover, it provides effective system analysis if the model is simulated under different operating conditions and with different system parameters [35]. In order to validate our hypothesis that speckle-tracking methods can generate perfusion mapping images and ultimately provide quantitative measurements of tissue perfusion this study uses a powerful software called Field II.

Field II was created by Jensen *et al.* [36,37] and it makes possible to model arbitrary transducers and to use realistic image scan sequencing. The approach is based on spatial impulse response estimation and makes use of linear system theory to determine the ultrasound field based on an excitation pulse, temporal impulse responses of the transmitting and receiving transducers, and the spatial impulse response at a given point.

Tissue is modeled as a collection of point scatterers and blood is modeled as a randomly distributed point scatterers that move during the simulation. Each ultrasound beam is simulated individually so it is possible to update the position of moving scatterers between beam acquisitions.

Computational fluid dynamics (CFD) played an important role in the simulation allowing the acquisition of realistic flow fields (blood) in complex geometries that are known to be related to physiological and pathological conditions. During development and validation of the proposed method vessel

wall movement was omitted. Still, the combination of CFD and ultrasound simulations allowed for a realistic understanding of blood perfusion.

This chapter makes use of a bottom up approach while having ultimate control of actual perfusion values for different microvasculature patterns. We started simulating blood flowing on straight tubes where it was relatively easy to calculate perfusion and prove that the proposed method is able to estimate blood perfusion and generate perfusion mapping images. Then, it moved on to more complex patterns such as kidney and tumor like vasculature. At that point only on plane vessels were considered, however, this is not very realistic since when estimating perfusion out of plane vessels have a crucial role. Therefore, a simulation using 3D random walk vessels was developed.

The effect of noise had to be analyzed for different vasculature depths. Ultrasound transducers add electronic noise to the system degrading SNR. Considering that blood flows very slowly in micro vessels, the electronic noise could degrade blood signal to the point that perfusion estimation would be compromised. To boost SNR we made use of Golay sequences and their effectiveness was investigated through simulations. The combination of block-wise SVD filter and the AM2D algorithm for tissue motion compensation increased perfusion sensitivity. Only after proving the robustness of the proposed method to estimate tissue perfusion the research moved forward to *in vivo* experiments.

We used Plane Wave Compounding (PWC) imaging which needs only few insonifications to reconstruct a full image [38]. This allows acquisition at a very high frame rate which increases the ensemble size and consequently increases signal-to-noise + clutter ratio when combined with SVD filters.

Finally, it was proven that, even though Power Doppler imaging is a very powerful tool in providing important morphological information it cannot provide information about blood perfusion in microvasculature evidencing the value of this research in estimating perfusion.

3.2 Plane Wave vs. Scan-Line Acquisition

Considering the bottom-up approach it was necessary to replicate the second order SVD filter (to be used with PWC imaging) and the high-order SVD filter (used on focused ultrasound imaging) mentioned on Chapter 2 Section 2.4.2 to decide what acquisition method to use. Both algorithms were first implemented by other research groups, but the algorithms were not open source.

When this research was initiated the papers about the block-wise SVD filter [23], which provides an adaptive method to isolate the blood subspace, and the statistical classifier proposed by Kim *et al.* [21], which is used to isolate the blood bandwidth when pulse-echo acquisition is used were not yet published. Therefore, the process of tuning an SVD filter was very meticulous to ensure that only the eigenvalues related to blood flow were being considered, which may differ depending on the application. An effort to automate the important eigenvalues was made and the use of machine learning was considered, but this work was not finalized by the time this research was completed.

Viti *et al.* [55] investigated the trade-off between SNR, resolution and framerate when plane-wave compounding and scan-line acquisition were used to image ultrasound contrast agents using the non-destructive model. Based on that research, on average, when compared with focused imaging, the use of plane-wave compounding showed a 10dB increase on contrast values when 63 angles were used and 7dB increase when 9 angles were compounded. Since higher contrast values are related to higher sensitivity to perfusion while suppressing tissue and noise signals, and that plane-wave compounding provide the capability of acquiring large datasets, PWC was the acquisition method of choice to be used throughout the research.

In PWC each plane wave k is emitted with a steering angle defined as $\alpha^k = \arcsin\left(\frac{k\lambda}{x_{lat}}\right), k\left\{-\frac{N_{pw}}{2}, \dots, \frac{N_{pw}}{2} - 1\right\}$. Where N_{pw} is the total number of waves to be emitted. The emission delays of the plane wave k for each element i of the transducer is as follows ${t_i}^k = (i-1)pitch * \tan(\alpha^k)/c$, where $pitch$ represents the distance

between the center of the two elements of the probe and c is the propagation speed of the ultrasound wave in soft tissues. The final PWC image is obtained by adding all the N_{pw} low resolution images [38].

The easiest way to understand and implement the SVD filter was to design simulations with straight tubes with a static background (to simulate tissue) and moving scatterers to simulate red blood cells. Speckles inside and outside the tube had the same density. To make the blood flow more realistic we used of CFD and, therefore, blood was flowing in a parabolic trajectory.

This simulation used a linear array with 256 lambda-pitch elements of center frequency 21MHz. Field II was used to model blood and tissue scatters, with the ratio between the amplitude of blood to stationary tissue set to 0.7. The largest velocity of scatterers was defined as 1mm/s, and the ultrasound propagation velocity in tissue was 1540m/s. Field II was used to simulated both scanline imaging and plane wave imaging (with 9 plane wave angles spanning -5 to +5 degrees). The acquired dataset was used to implement the second order SVD filter algorithm used in this research.

3.3 Perfusion Mapping

Before moving forward with simulations that mimicked real life microvasculature, we had to define what method for estimating speckle decorrelation would be best suited for the proposed application. We investigated two methods, one based on the width of the autocorrelation function of each pixel in time (Method 1) and the second that fitted the main-lobe of the autocorrelation function to a Gaussian parameterized by the standard deviation (Method 2). In the latter the standard deviation is defined as the reciprocal of the speckle-decorrelation rate. Figure 3.1 illustrates how the autocorrelation function was obtained.

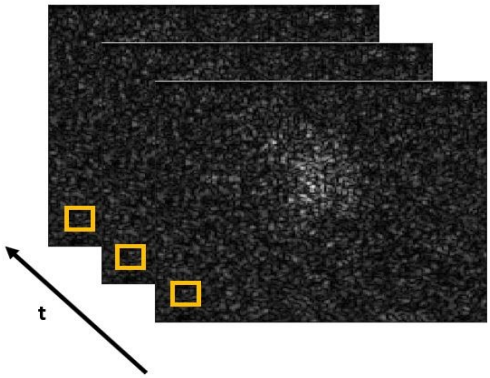

Figure 3.1 – Illustration of data frames used to calculate autocorrelation function in time.

In order to decide which method would provide the best estimation for the speckle-decorrelation rate we ran a series of experiments. The setup shown in Figure 3.2 was used to acquire ultrasound data that was later used to estimate speckle decorrelation. The ultrasound transducer was placed on top the sample for water coupling.

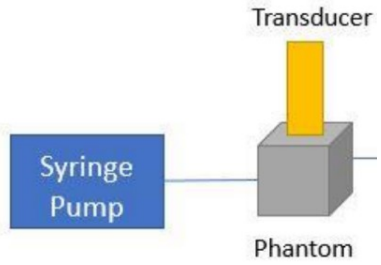

Figure 3.2 – System setup for imaging the flow phantom. Flow speed is the controlled variable and preset at the syringe pump.

The experiments were performed on a flow phantom and transparent polyurethane tubing (SAI Infusion Technologies, IL, USA) with inner diameter (ID) of 1.016mm was used to mimic a blood vessel. One vessel was embedded at 5mm deep inside the phantom. A non-scattering phantom composed of 10%

gelatin by mass was used. The fluid flowing through the tube was a mixture of water and cornstarch that mimics blood flow dynamics. The syringe pump was used to setup speed flow varying from 1mm/s to 10mm/s. A linear array transducer LZ250 (Fujifilm, VisualSonics, Inc.) combined with the Verasonics Vantage 256 (Verasonics, Inc.) ultrasound acquisition system was used.

Several sets of data were acquired and later processed using MATLAB (The MathWorks, Inc., Natick, MA, USA).

Firstly, we used Method 1 to estimate speckle-decorrelation. Figure 3.3 shows the difference in width for a static point outside of the tube (Point 2), and for a moving point inside of the tube (Point 1). The width of the autocorrelation function decreases as an inverse proportion of fluid flow. However, the several lobes made it difficult to define what width would best characterize speckle-decorrelation rate. Still, we were able to appropriately differentiate the speckle-decorrelation for higher and lower speed flows as can be seen on Figure 3.4.

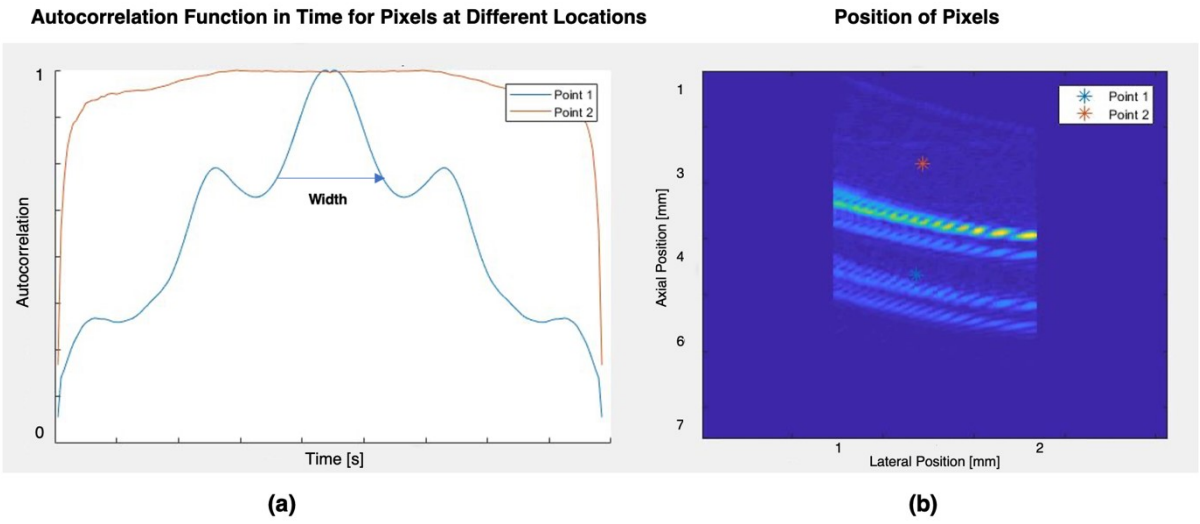

Figure 3.3 – Left: Autocorrelation function in time for a location outside the flow tube (Point 2) and for a location inside of the tube (Point 1). Right: B-mode scanline image showing the two point locations.

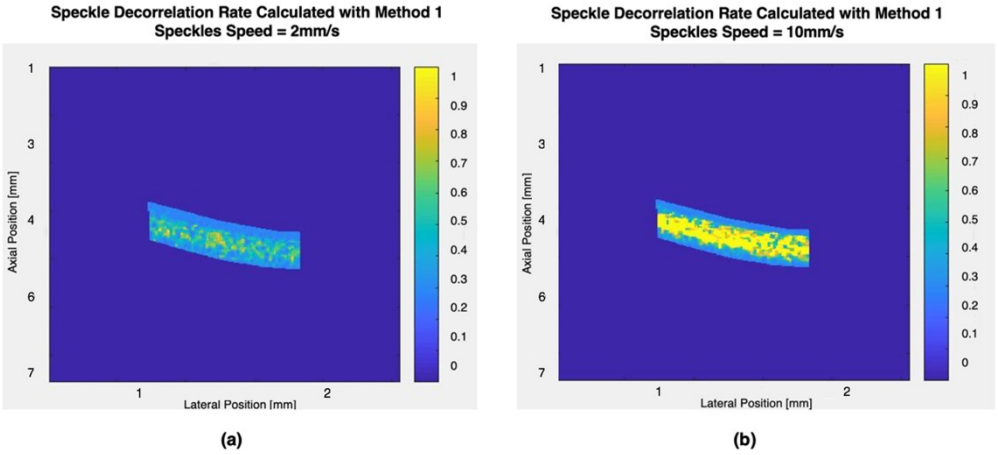

Figure 3.4 – Speckle-decorrelation rate calculated using Method 1 (a) for speckles moving at 2mm/s (b) for speckles moving at 10mm/s. Colormap represents the normalized speckle-decorrelation rate.

Secondly, we used Method 2 to estimate speckle-decorrelation. This method proved to be more robust and to minimize noise interference when instead of fitting the autocorrelation curve of one pixel in time, we analyzed the autocorrelation function on a square window of pixels (4x4). Figure 3.5 shows the Gaussian curve parametrized by the standard deviation that was used to calculate the speckle decorrelation rate. Figure 3.6 shows the estimated speckle decorrelation rate for different blood flows when Method 2 was used.

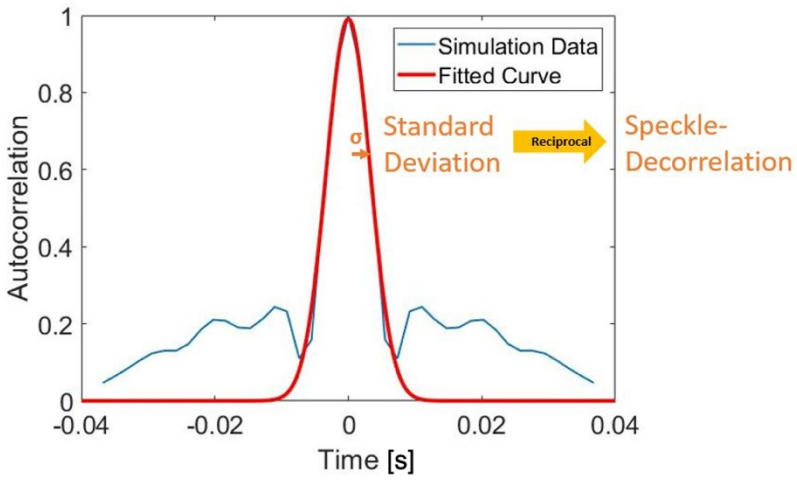

Figure 3.5 – Description of Method 2: autocorrelation function fitted with a Gaussian curve parametrized by the standard deviation. The speckle-decorrelation rate is defined as the reciprocal of the standard deviation.

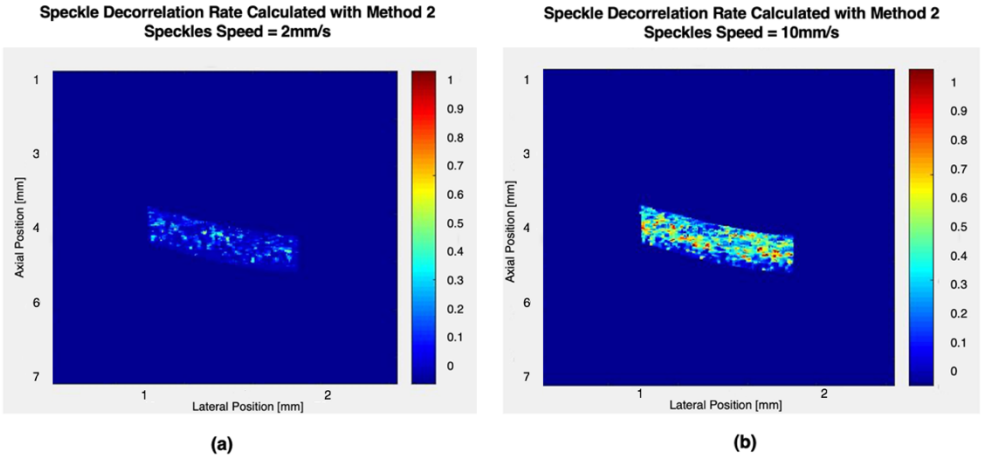

Figure 3.6 – Speckle-decorrelation rate calculated using Method 2 (a) for speckles moving at 2mm/s (b) for speckles moving at 10mm/s. Colormap represents the normalized speckle-decorrelation rate.

To validate Method 2 even further we expanded the phantom experiment by using a tissue mimicking phantom composed of 10% gelatin and 10% cornstarch

by mass, which provides ultrasonic and mechanical properties similar to human tissue [29]. We also used a transparent polyurethane tubing (SAI Infusion Technologies, IL, USA) with inner diameter (ID) of 0.0348mm to mimic a blood vessel 5mm deep into the phantom. This time we used blood as fluid and used Method 2 to estimate the speckle-decorrelation rate. We filtered the dataset using the proposed second-order SVD filter algorithm we implemented. Figure 3.7 show the results.

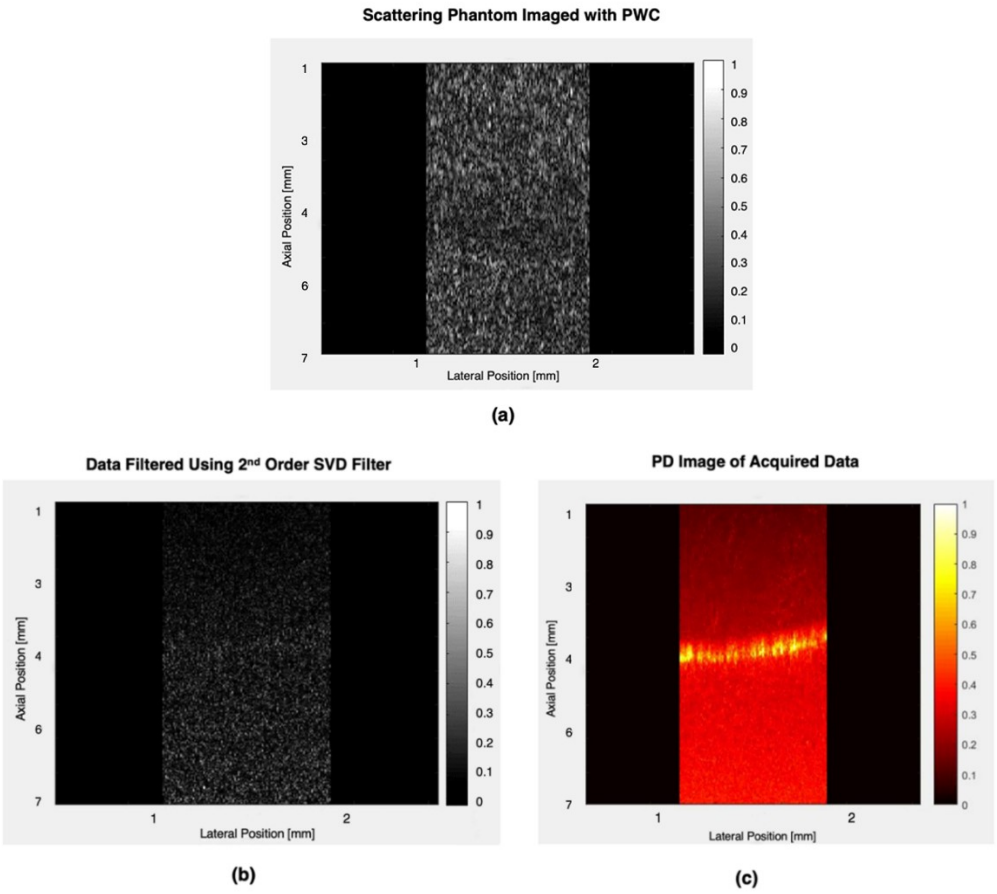

Figure 3.7 – Scattering phantom imaged using plane wave compounding image (a) original data frame (b) data filtered using second-order SVD filter (c) PD image of the acquired data. Gray colormap represents the ultrasound backscattered signal normalized and the hot colormap represents the normalized PD signal.

This validated Method 2 as the method of choice for calculating the speckle-decorrelation rate for the rest of this research.

3.3.1 2D Microvasculature

Karshafian *et al.* [39] proposed two vascular models that represent "kidney-like" and "tumour-like" structures using rules of branching and fractal geometry in two dimensions. These structures are proven to match networks of real kidney and tumour vascular trees and therefore are a great tool to simulate microvasculature characterized by small size (<50μm diameter) and blood speeds of less than 1mm/s.

By simulating microvasculature that mimics real life structure we can test our hypothesis that high-frequency ultrafast ultrasound combined with the proposed perfusion mapping algorithm can estimate blood perfusion without contrast agents.

The computational vascular network model proposed by Karshafian *et al.* [39], is based on two principles that can be summarized as follows. Firstly, both vascular networks (kidney and tumour like) have a fractal-like branching where a parent vessel bifurcates into daughter vessels of shorter lengths, a process that is repeated successionally. Secondly, the total resistance of the system is minimized which provides a relationship for the diameter of vessels at the bifurcation.

The difference between generating a "tumour-like" and a "kidney-like" structure lies in changing parameters such as vessel diameter, length and branching angle.

The relationship between the diameter of a parent vessel (D_0) and its daughter vessels (D_1 and D_2) is given as [39]:

$$D_0^{\gamma} = D_1^{\gamma} + D_2^{\gamma} \quad (3.1)$$

Where γ represents is the bifurcating exponent and assumed to be 3.

The symmetry of the daughter vessels is given by the bifurcation index (β) defined as [39]:

$$\beta = \frac{D_1}{D_2} \quad (3.2)$$

Real life vascular structures are asymmetric, therefore, we assume that the diameters of the daughter vessels are different. In this research we assume β=0.95.

The length of each daughter vessel is proportional to the length of a parent vessel by a factor *k* as seen on Equation 3.3 [39]. *k* is set for simulation purposes to 0.9 +/- a length span to add a degree of randomness. For "kidney-like" structures the length span was 0.05 and for "tumour-like" structures the length span was 0.1.

$$L_{daughter} = kL_{parent} \quad (3.3)$$

A uniformly distributed function is used to assign branching angles in the vascular models. For "kidney-like" structures branching angles vary from 25.50° to 28.50°, but for "tumour-like" structure since a random like structure is desired branch angles vary from 25° to 140°.

The network hemodynamics is assumed to be steady, laminar flow of varying viscosity and the vessels are assumed to be rigid, cylindrical and impermeable. Poiseuille's law is used to estimate flow resistance. This model accounts for several effects such as the Fahraeus-Lindqvist effect that states the dependence of the apparent viscosity of blood flow based on vessel diameter and the Fahraeus effect that states the reduction of intravascular hematocrit relative to the inflow of a vessel [40].

To create tumour like and Kidney like vasculature the initial conditions had to be changed and are shown in Table 3.1. Parameters changed based on the type of vasculature we were analyzing. We had to combine this network morphology

and hemodynamics with the Field II software so we could use ultrasound theory to acquire data using plane wave compounding imaging while blood was flowing through the structure.

Parameter	Degree of Randomness	
	Kidney	Tumour
Length	85-95%	80-100%
Diameter	95-105%	90-110%
Angle	25.5°-28.5°	25°-140°

Table 3.1 Global parameters used to generate "kidney-like" and "tumour-like" random walk microvasculature.

To implement the microvascular beds in Field II we had to define some global parameters based on the information in Table 3.1. For both "kidney-like" and "tumour-like" microvasculature the maximum node length was set to be 2.5mm, the maximum diameter was 500μm and the minimum diameter was set to 5μm. The bifurcation exponent is $\gamma = 3$ and the bifurcation index (related to the asymmetry in diameters) is $\beta = 0.95$ with a randomness asymmetry constant of 0.04. We had 100,000 scatterers flowing through the microvasculature at all times.

To define flow through the vasculature we must define the flow through the root vessel which was done by defining the volumetric flow [m^3/s] in the fist vessel. The volumetric flow ranged from 0.1mm^3/s to 5mm^3/s in most simulations.

The flow speed in each vessel is calculated by dividing the volumetric flow by the area of the node (all the relevant parameters of a node including diameter were stored in the "vascular" object in Matlab). The velocity of each scatterer depends on the framerate and it is constant for the same width, that is if the scatterer is travelling through the same node. The scatterer velocity is used to calculate the position of speckles on each frame.

Pressure at each node was calculated based on the principle of conservation of mass where the volumetric flow from the two daughters must be equal to the volumetric flow on the parent node. The flow resistance was calculated based on Equation 4 presented in Karshafian *et al.* [39].

The number of nodes will vary from simulation to simulation since we will keep generating daughter nodes until their diameter is smaller than the minimum diameter specified.

The scatterers are populated in the microvasculature based on a randomly chosen "radius position" that is normalized to the diameter of the vessel, which will be constant throughout the entire run for the scatterer. Scatterers will move towards the next node with a parabolic velocity profile and when reaching a node it will randomly choose which vessel it will continue on. This choice is weighed towards the vessel with higher flow speeds. Moreover, when the vessels get really small the RBCs tend to choose only one vessel to travel to. The scatterers positions are collected to be used with Field II.

To image the microvasculature we used a linear array with 256 lambda-pitch elements of center frequency 21MHz. The pulse repetition rate was adjusted for different simulations and scatterers positions were updated between acquisitions.

Several microvascular beds for both kidney-like (Figure 3.8) and tumour-like (Figure 3.9) microvasculature were created with different velocities. We used the proposed perfusion rate estimation method on each simulation to analyze the relationship between the correlation coefficient and the change in flow speed to ensure it was possible to estimate tissue perfusion from speckle decorrelation rate.

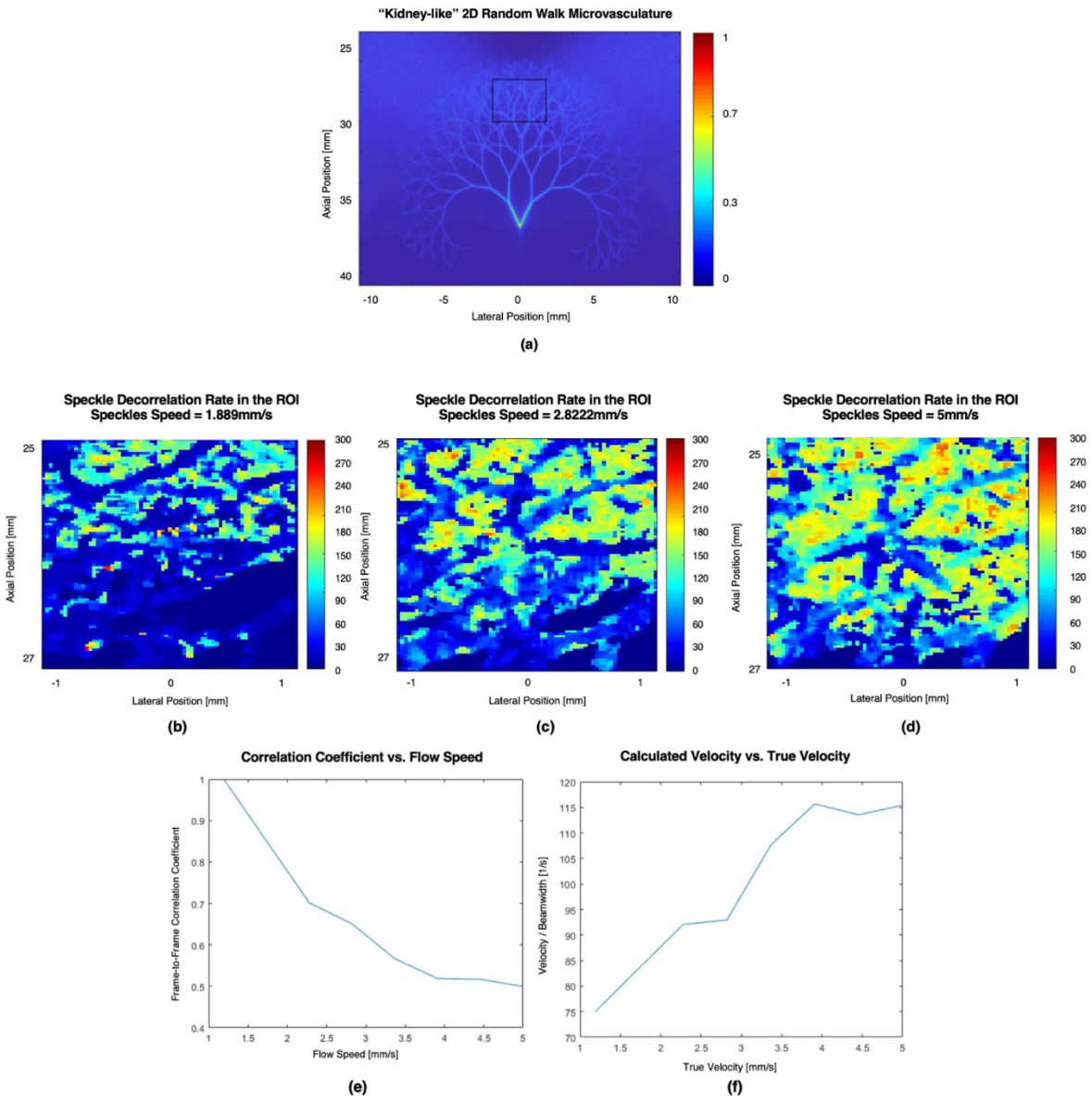

Figure 3.8 – 2D random walk microvasculature (a) "Kidney-like" structure where colormap represents the normalized PD signal (b) Perfusion mapping at the ROI shown in Figure 3.9(a) for speckles moving at 1.889mm/s (c) Perfusion mapping at the ROI shown in Figure 3.9(a) for speckles moving at 2.8222mm/s (d) Perfusion mapping at the ROI shown in Figure 3.9(a) for speckles moving at 5mm/s (e) correlation coefficient as a function of the flow speed (f) calculated velocity vs. true velocity. Colormap on figures (b), (c), and (d) represents the speckle-decorrelation rate. In the pictures speckles speeds refers to the volumetric flow at the root node.

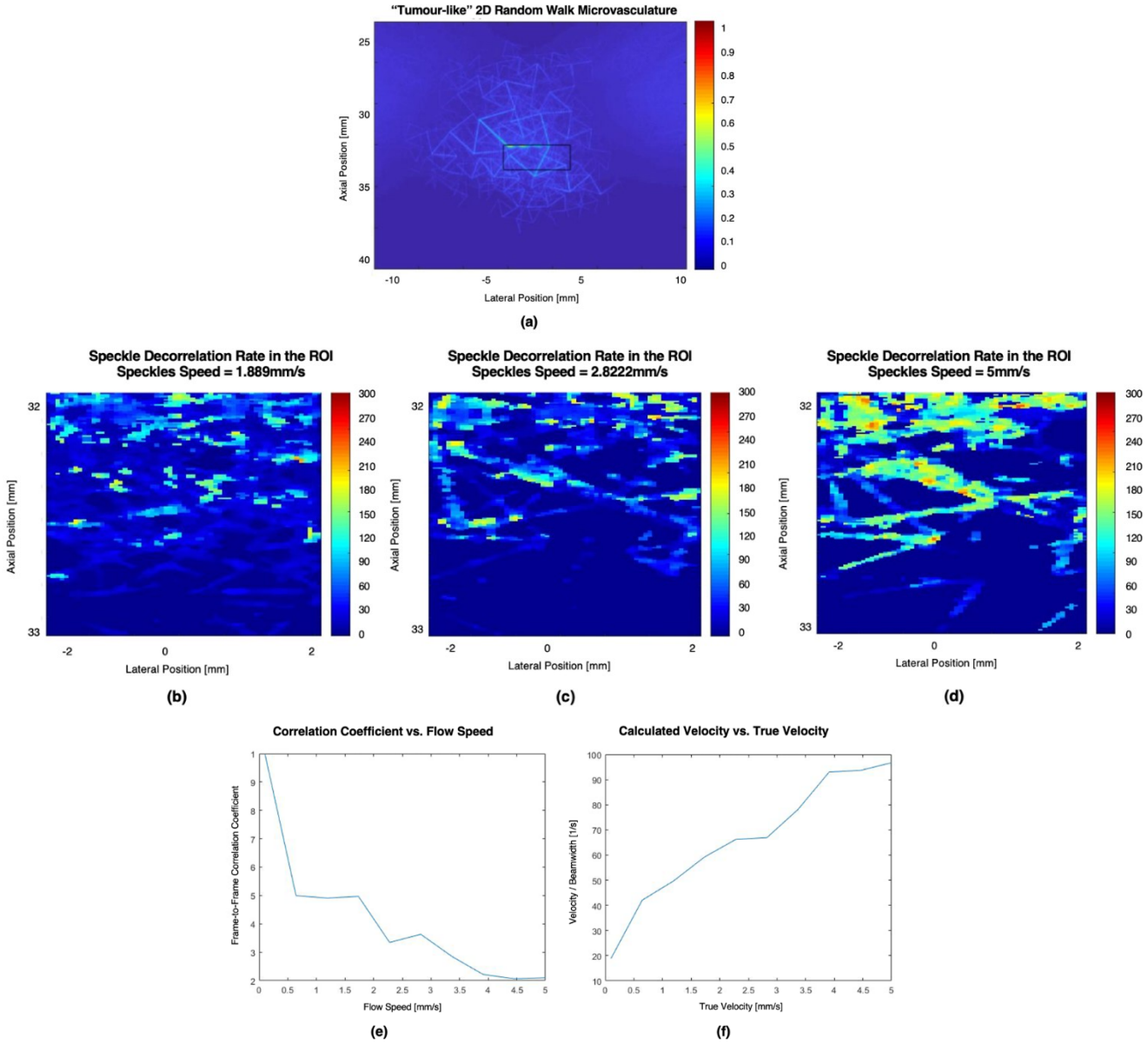

Figure 3.9 - 2D random walk microvasculature (a) "Tumour-like" structure where colormap represents the normalized PD signal (b) Perfusion mapping at the ROI shown in Figure 3.9(a) for speckles moving at 1.889mm/s (c) Perfusion mapping at the ROI shown in Figure 3.9(a) for speckles moving at 2.8222mm/s (d) Perfusion mapping at the ROI shown in Figure 3.9(a) for speckles moving at 5mm/s (e) correlation coefficient as a function of the flow speed (f) calculated velocity vs. true velocity. Colormap on figures (b), (c), and (d) represents the speckle-decorrelation rate. In the pictures speckles speeds refers to the volumetric flow at the root node.

The ratio that represents the calculated velocity (velocity / beamwidth) in Figures 3.8(f) and 3.9(f) were calculated using Equation 3.5 [101] that states that the normalized autocorrelation function modelled by a Gaussian curve is proportional to flow speed.

$$Autocorrelation \sim \exp\left(-\frac{\Delta t^2}{2}\left|\frac{V}{\sigma(y)}\right|^2\right) \quad (3.5)$$

Where Δt is the framerate, V is the fluid velocity and σ(y) is the beamwidth [101]. When plane-wave imaging was used σ is considered the lateral width of the received point spread function (PSF).

The results in Figure 3.8 (e) and Figure 3.9 (e) that evidenced that the correlation coefficient is inversely related to the flow speed as we were expecting. Therefore, we could compare the estimated perfusion (speckle-decorrelation rate) with the calculated perfusion (Equation 3.4).

$$Perfusion_{Calculated} = \frac{ScattererFlow}{Area\ of\ ROI} \quad (3.4)$$

Here scatterer flow is defined as the number of scatterers crossing the boundary of a ROI per unit time.

For several simulations we compared the calculated and estimated perfusion (speckle-decorrelation rate) to validate the proposed method. For each simulation indicated in Figure 3.10(d) and 3.10(e) scatterers had the same volumetric flow at the root node, and only like structures were compared ("kidney-like" and "tumour like"). However, due to the degree of randomness on each structure no two like structures were exactly the same, which added to the level of robustness since in clinical situations the microvasculature is not identical on different subjects.

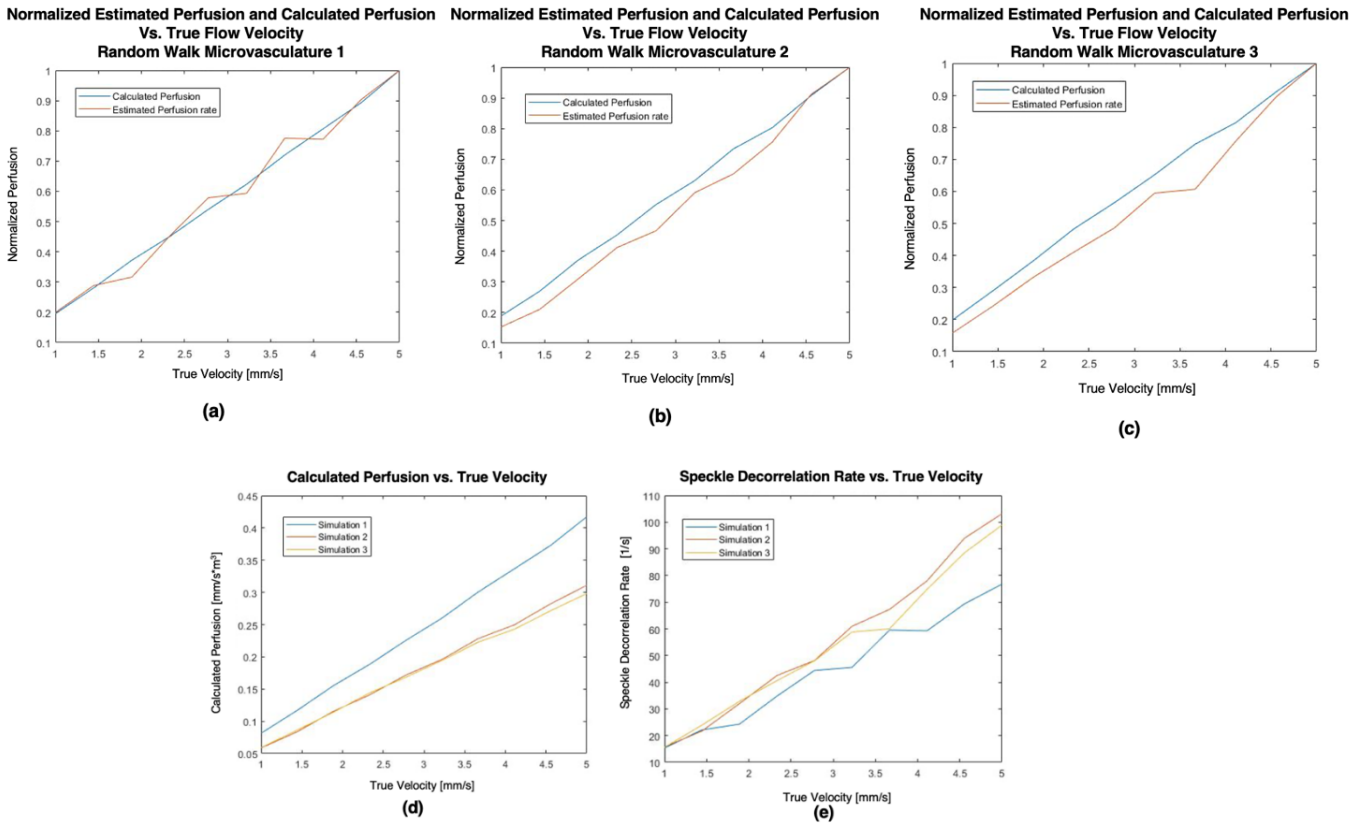

Figure 3.10 – Calculated perfusion and estimated perfusion as a function of the true velocity for three different 2D tumour-like random walk microvasculature generated using like parameters (a) Random Walk Microvasculature 1 (b) Random Walk Microvasculature 2 (c) Random Walk Microvasculature 3 (d) Calculated Perfusion as a function of the true velocity on all 3 Microvasculature (e) Estimated Perfusion as a function of the true velocity on all 3 Microvasculature.

The simulation results shown in Figure 3.10 demonstrate that for "kidney-like" and "tumour-like" microvascular cases speckle-decorrelation rate follow similar trends with true perfusion rate over a range of root vessel velocities.

The statistical analysis provides an overview about the relationship between frame rate, maximum and minimum detectable speeds and the number of frames needed to provide a good perfusion estimation. The results can be seen on Table 3.2.

Frame Rate (Hz)	**Min. Speed (mm/s)**	**Max. Speed (mm/s)**	**Number of Frames**
10	-	-	-
25	0.1	0.5	50
50	0.1	0.8	100
100	0.1	2	50-200
250	0.1	4.5	250-500
500	0.1	10	500-1000

Table 3.2 – Blood flow sensitivity as a function of frame-rate for datasets coming from the same population ("tumour-like" 2D random walk microvasculature).

It is possible to notice that the higher the frame rate the greater the maximum detectable flow speed. Moreover, increasing the framerate and the number of frames acquired improves the robustness of the proposed method to a certain extent as per Figure 3.11. That is consistent with other studies that showed that the increase in ensemble size is related to a better perfusion sensitivity when SVD based filters were used.

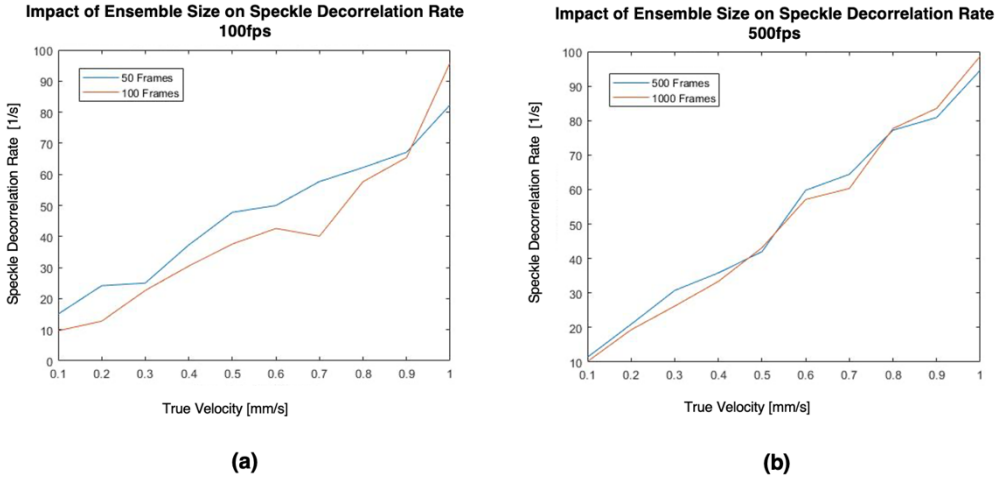

Figure 3.11 - Speckle-decorrelation rate as a function of the true velocity (a) for frame rate =100Hz (b) for frame-rate = 500Hz.

We also analyzed the impact of noise on perfusion measurements since good SNR is crucial for perfusion sensitivity. Therefore, investigating the minimum SNR required for calculating speckle decorrelation rates was an important limiting factor. The SNR was calculated as the reciprocal of the coefficient of variation (CV).

$$CV = \frac{\sigma}{\mu} \quad (3.6)$$

Where σ is the population standard deviation and μ is the population mean. It is possible to notice based on Figure 3.12 that increasing the noise in the system hinders the capability of the proposed method in estimating tissue perfusion and the minimum SNR required for estimating tissue perfusion was found to be 2.3dB. Later on, in an attempt to improve SNR we implemented the adaptive block-wise SVD filter (to increase SNCR) and used Golay sequences.

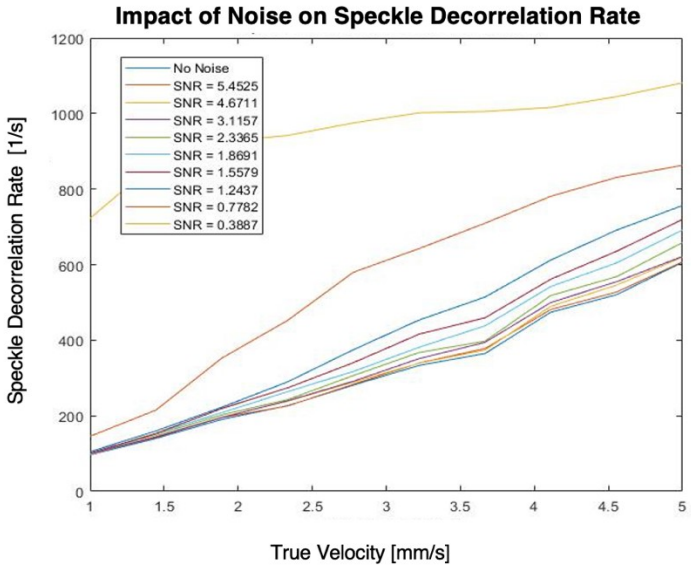

Figure 3.12 – Impact of noise on estimating the speckle-decorrelation rate.

3.3.2 3D Microvasculature

Up to this point we used the Karshafian *et al.* [39] study to create 2D microvascular structures. However, in reality, the microvasculature is composed of "on plane" and "out of plane" vessels. To address this issue we had to expand their study to create a 3D microvasculature as shown on Figure 3.13. Figure 3.14 shows the US image of a 3D random walk microvasculature.

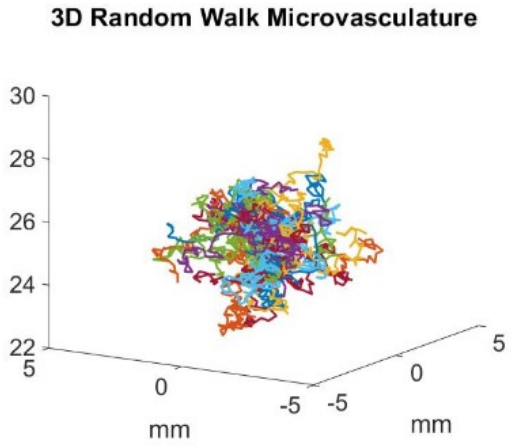

Figure 3.13 – 3D "Tumour- Like" random walk microvasculature mimicking the disorganized microvasculature of a tumor.

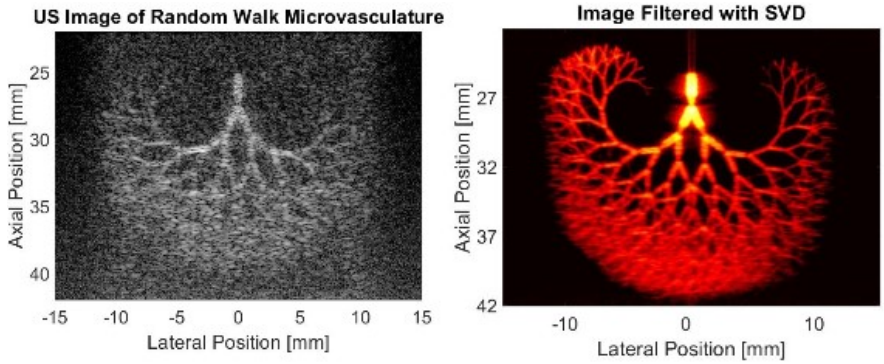

Figure 3.14 – 3D random walk microvasculature mimicking "kidney-like" structure (a) US image (b) PD image.

The new calculated perfusion is shown on Equation 3.7.

$$Perfusion_{Calculated} = \frac{ScattererFlux}{Volume\ of\ ROI} \quad (3.7)$$

Analysis of the new simulation showed that the proposed method to estimate tissue perfusion was robust even when 3D microvascular structures were analyzed. Therefore, the hypothesis that the speckle decorrelation rate can be used to estimate tissue perfusion was validated even when "out of plane" vessels were imaged, a case that satisfies real life scenarios and exposes the value of the proposed method to estimate tissue perfusion for clinical applications. Figure 3.15 shows the perfusion mapping for the true perfusion rate and the speckle decorrelation rate while Figure 3.16 shows the relationship between speckle-decorrelation rate and calculated perfusion. We performed a linear regression that indicates a relationship with a correlation $R^2 = 0.98$.

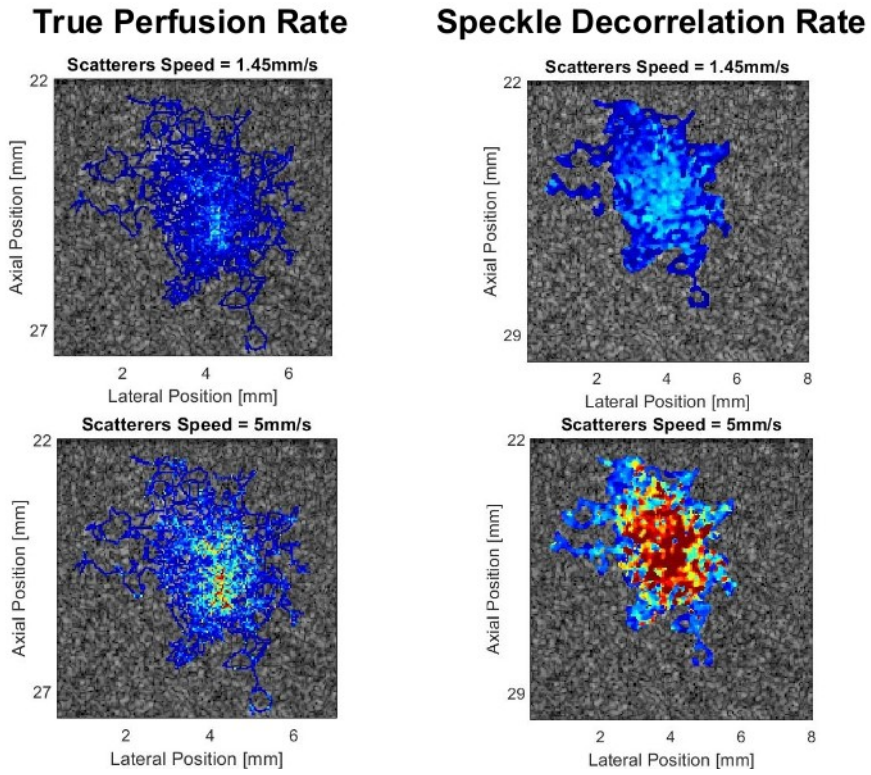

Figure 3.15 – Perfusion mapping comparing true perfusion rate calculated using Equation 3.6 and the speckle-decorrelation rate calculated using the proposed method.

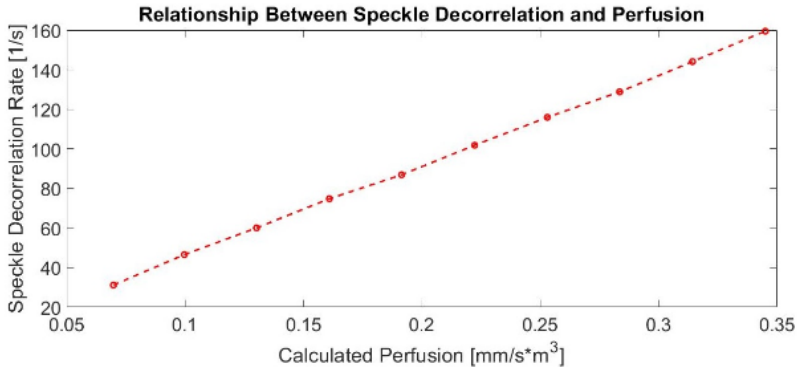

Figure 3.16 – Relationship between speckle-decorrelation rate and calculated perfusion.

We also added noise and tunned our clutter filter to suppress the last eigenvalues which are known to be related to noise. However, the size of the blood subspace was defined arbitrarily and on an attempt of automating this process we implemented our version of the adaptive block-wise SVD filter that defines the size of the blood subspace on small windows rather than on the full image.

In Figure 3.17(a) we made use of a 1st order SVD filter that relies on the fact that a matrix with full rank can be approximated by another with lower rank through Singular Value Decomposition [79]. Assuming that we have a matrix $\boldsymbol{A}$ with rank r that can be approximated to one of lower rank $\tilde{\boldsymbol{A}} = \boldsymbol{U_s \Sigma_s V^*}$, $s < r$, where "*" denotes the conjugate transpose, $\boldsymbol{U_s}$ and $\boldsymbol{V_s}$ are the orthogonal matrices and $\boldsymbol{\Sigma_s}$ is a diagonal matrix of singular values σ_I sorted in descending order. The matrix $\tilde{\boldsymbol{A}}$ is the best approximation of $\mathbf{A}$ in the least square sense $||\boldsymbol{A} - \tilde{\boldsymbol{A}}||^2$.

For the implementation of the first order SVD filter, one needs to first reshape the acquired 3D ultrasound data to a spatiotemporal matrix form as was done in [22]. This is achieved by transforming the 3D dataset consisting of dimensions (N_z, N_x, N_t) into a 2D spatiotemporal matrix of dimensions (N_z x N_x, N_t). One can now apply singular value decomposition (SVD) to this matrix to deconstruct it to its eigenimages.

As mentioned in Section 2.4.2, it is commonly assumed that tissue scattering is more echogenic than blood scattering [102] and that tissue and blood

contribute more to the variance than noise. Therefore, we can assume that the first eigenvalues in $\boldsymbol{\Sigma_s}$ belong to tissue, followed by blood and noise. We can obtain an image of the blood signal by simply zeroing the tissue and noise eigenvalues. Thus, the lower rank approximation matrix containing only the eigen-images belonging to the blood subspace can be represented by the following: $\tilde{A} = \sum_{i=c+1}^{c+d} \boldsymbol{\sigma_i u_i v_i^*}$.

Where c and d represent the rank of the clutter and blood signal. This can be thought of as decomposing our spatiotemporal matrix into a weighted, ordered sum of separable matrices A_i (eigen-images). Moreover, u_i and v_i are the i^{th} column of the corresponding SVD matrices, and σ_i are the ordered singular values. It is important to keep in mind that each column v_i corresponds to a temporal signal with length N_t and each column u_i corresponds to a spatial signal with length N_t. The overlay in Figure 3.17(a) represents the eigen-image belonging to the blood subspace when first order SVD filter is used.

Figure 3.17(b) represents the eigen-image of the blood subspace when the second order SVD filter is used. This filter is very similar to the first order SVD, however, rather than having only regular frames the dataset is composed of super frames and in our simulations each super frame was a collection of 15 frames.

Therefore, we would exercise the same process used for the first order SVD filter on each super-frame (set of 15 frames) and only then we would apply the SVD filter on the eigen-images from the super-frames. Applying the SVD filter twice on the dataset proved to increase perfusion sensitivity.

However, due to the lack of a standardized approach to choosing the proper eigenvalues, selecting the optimal thresholds that separate the clutter-blood and blood-noise interface was a challenge especially when noise was added as can be seen in Figure 3.17(a) and Figure 3.17(b) where it is evident the existence of signal unrelated to tissue perfusion surrounding the “tumour-like” microvasculature.

To overcome this challenge, we made use of the block-wise SVD filter that adaptively define the eigenvalues related to the clutter-blood and blood-noise interface based on local data statistics [23].

Song *et al.* [23] proposed the use of two clutter filtering approaches to adaptively determine the eigenvalue representing the interface between clutter and blood. First, the gradient of the singular value curve was analyzed and the turning point was identified (cutoff 1A). Second, the curve of mean Doppler frequency of each singular vector (related to vectors **V**) was analyzed and cutoff 1B was identified as the singular value above a pre-defined tissue motion frequency threshold. The greater of cutoff 1A and cutoff 1B was chosen as the proper eigenvalue to represent the clutter-blood interface.

To determine the eigenvalue related to the blood-noise interface it was assumed a Gaussian noise distribution throughout the local data. Therefore, the eigenvalues related to noise should follow a linear distribution in the logarithm scale (gradient of the singular value curve). By linear fitting the tail of the gradient of the singular value curve it was possible to identify the point where the curve deviates from the linear fitting and that will be considered the eigenvalue representing the blood-noise interface [23].

For each block in the original dataset, the blood subspace is defined using the adaptive method proposed by Song *et al.* [23] to identify the eigenvalues related to the clutter-blood and blood-noise interface. Moreover, an inverse SVD calculation described by Equation 3.8 must be performed to calculate the blood flow signal *S(x, z)* for each pixel.

$$S(x,z) = \frac{1}{N}\sum_{n=1}^{N} \frac{S_n}{\sum_{Low\ cutoff}^{High-cutoff} \lambda} \quad (3.8)$$

Where N is the total number of overlapped blocks containing the target pixel (x, z), S_n is the clutter-filtered signal from block n, and λ are the remaining eigenvalues related to blood signal.

The use of the adaptive block-wise SVD filter considerably increased perfusion sensitivity as can be seen in Figure 3.17 (c). Furthermore, the use of the block-wise SVD filter allowed us to keep the spatial resolution since spatial

averaging similar to the one described on Section 3.3 (4x4 windows combined with 2nd order SVD filter) was no longer required.

Despite the great advances in adaptively choosing proper threshold values, the method proposed by Song *et al.* [23] had limitations related to the arbitrary choice of the tissue motion frequency threshold and the block size. To estimate the optimal block-size and block overlap percentage we had to consider that if the block size is too big the noise variance may change in the ROI and if the block size is too small ($n_x * n_z < n_t$) we would face insufficient degrees of freedom. Determining the block overlap is a trade-off between image quality and computational cost.

We investigated the optimal block size and block overlap for our application, and for the ensemble size of the simulated data (500 frames) a block-size of 80 was chosen and the block overlap was set to be 85%.

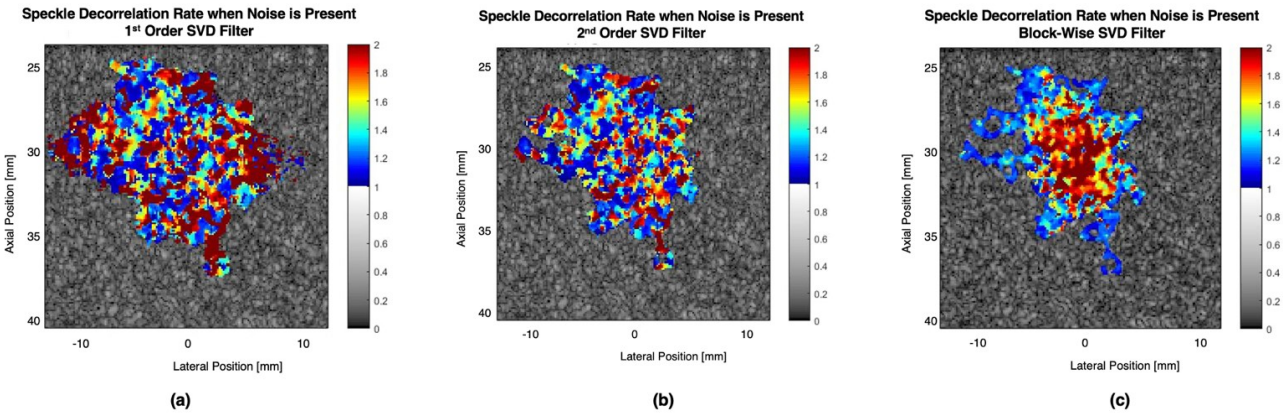

Figure 3.17 – Effectiveness of the adaptive block-wise SVD filter in isolating the blood subspace (a) when data is filtered used 1st Order SVD Filter (b) when data is filtered using 2nd Order SVD Filter (c) when data is filtered used Block-Wise SVD Filter. Gray colormap represents the normalized ultrasound backscattered signal and the overlay represents the normalized speckle decorrelation rate.

Upon initial *in vivo* experiments we were faced with an issue when tissue motion was on the same magnitude as blood flow. Moreover, just the movement of the transducer was affecting speckle decorrelation rate estimation.

Therefore, we made use of the AM2D [60] algorithm to calculate axial and lateral displacements. This algorithm was applied on the RF data of one specific frame the frame immediately after to create the ultrasound deformation map. This deformation map was used to properly define the autocorrelation function in time and consequently better estimate the speckle decorrelation rate.

Moreover, the AM2D algorithm improved the capability of the block-wise SVD filter since by tracking tissue motion it is possible to better reorganize the 3D dataset into the 2D spatiotemporal matrix used to perform the singular value decomposition. We validated the AM2D algorithm on a 3D random walk microvasculature. Considerable motion to the background speckles was added to simulate tissue motion and movement of the transducer. Using the second order SVD alone in order to create PD images was not sufficient to suppress tissue motion with similar order of magnitude as blood flow as can be seen on Figure 3.18(b). However, combining block-wise SVD filter and the with the AM2D algorithm increased sensitivity which consequently increased the performance of the proposed method in estimating speckle decorrelation rate.

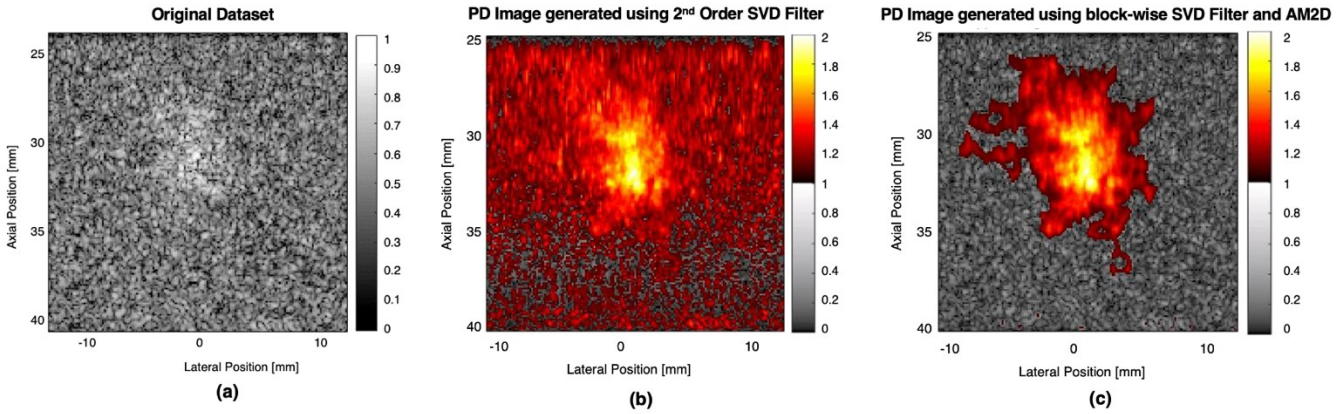

Figure 3.18 – 3D random walk microvasculature with tissue motion (a) original dataset (b) PD image generated using second-order SVD filter (c) PD image generated using the adaptive block-wise SVD filter in combination with the AM2D algorithm. Gray colormap represents the ultrasound backscattered signal normalized and the overlay represents the normalized PD signal.

3.4 Golay Encoding

The implementation of the block-wise SVD filter improved the robustness of the proposed method to noise. However, this algorithm considers the noise strictly as Gaussian noise which is not the best approach to simulate the spatially varying and complex noise seen *in vivo*.

Therefore, we hypothesized that Golay codes can increase perfusion sensitivity for the proposed method especially on *in vivo* experiments.

Golay sequences are suitable for ultrasound applications because of their complementarity property, which limits side lobe levels. If we suppose $a = a_0, a_1, \ldots, a_{n-1}$ and $b=b_0, b_1, \ldots, b_{n-1}$, to be a pair of Golay binary sequences of length n bits with $a_j, b_j \in \{-1,1\}$. Since a and b are complementary then:

$$R_{aa}(j) + R_{bb}(j) = 2n\delta \quad (3.7)$$

Where $R_{aa}(j)$ and $R_{bb}(j)$ represent the autocorrelation products of sequences a and b respectively, and $\delta(j)$ is the delta function. However, in order to emit a plane wave that carries the sequences a or b, these binary codes need to be modulated at a central frequency inside the bandwidth of the ultrasound probe [40]. The modulation chosen in this study is the Binary Phase Shift Keying (BPPSK) technique which consists in shifting the phase of a sinusoid (carrier) between two possible values 0 and π corresponding respectively to the code bit 1 or -1.

Therefore, the data acquisition is performed in two different steps, one for each plane wave k (as described in Section 3.2). Firstly, the signal related to the first Golay sequence a is emitted by the probe and backscattered signal $y_a(t)$ is recorded. Secondly, the signal related to the Golay sequence b is emitted and new backscattered signal $y_b(t)$ is recorded. In order to perform the pulse compression, one needs to assume the medium does not move between the two acquisitions, so the proper matching filter can be applied to each of the backscattered signals. After pulse compression the signals can be added to obtain the final image.

A 3D random-walk microvasculature phantom was created similar to the microvasculature described on Section 3.3.2. Scatterers were moving at different speeds, and ground truth perfusion was calculated based on Equation 3.7. Phantoms for scatterers moving from 1mm/s to 5mm/s were created.

All simulations were performed for a 256-element linear transducer array excited by one sine cycle burst pulse at nominal frequency of 21MHz. The echo signals are sampled independently at a frequency of 100MHz. The data was acquired at 500 frames per second.

The microvasculature phantom was imaged by using one cycle plane wave imaging as well as by using complementary Golay pairs of length 8 and 16 bits. The effect of the noise for every case is shown on Table 3.3. The standard

deviation of the noise was chosen based on the linear value of the IQ beamformed data.

Standard Deviation of Noise	SNR - One cycle excitation	SNR- Golay 8 bits	SNR- Golay 16 bits
2.02 x 10-25	-3dB	7dB	11dB
6.93 x 10-26	6dB	16dB	21dB
1.24 x 10-26	20dB	31dB	36dB
3.99 x 10-27	30dB	41dB	46dB
1.24 x 10-27	40dB	51dB	55dB

Table 3.3 – Comparison of SNR between one cycle plane wave imaging and Golay code plane wave imaging.

From Table 3.3 it is possible to see that the use of Golay sequences increase the signal to noise ratio. In general, the use of an 8-bit Golay sequence increased SNR in 10dB, while the use of a 16-bit Golay sequence increased SNR in 15dB when compared to one cycle excitation plane wave imaging. The difference in SNR resulting from doubling the length of the Golay sequence is reasonable since theoretically it would provide an increase of 6dB (SNR=20log10(2)). However, we would expect an increase of about 24dB (SNR = 20log10(16)) and not 15dB when 16-bit Golay sequences are used, therefore, it is reasonable to say that plane wave compounding has an effect on the final SNR, a problem that could lead to a full research by itself, and therefore it is not further analysed at this point.

The speckle-decorrelation rate was calculated using the data from one cycle excitation and for 16-bit Golay sequences when no noise was added. The results were then compared with the calculated perfusion and the results are consistent since there is no noise and therefore no increase in SNR is seen when Golay 16-bits sequences are used (Figure 3.19).

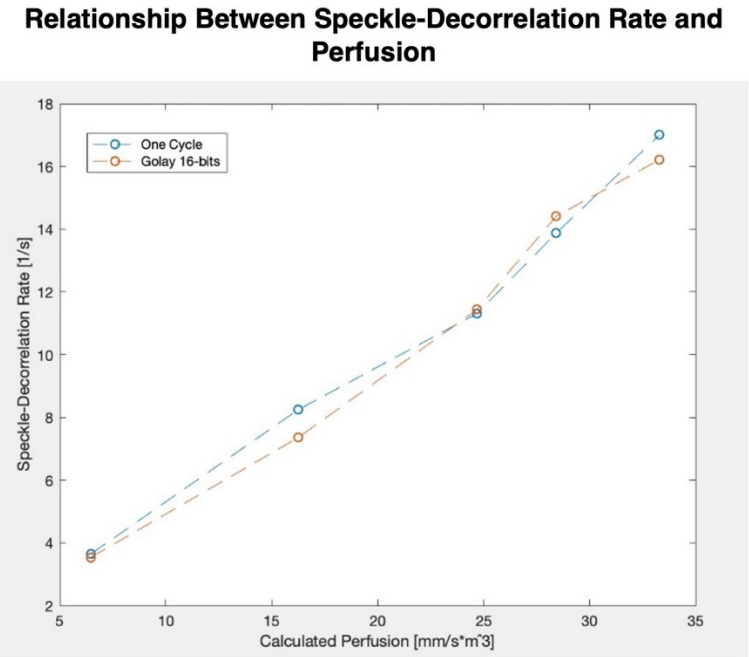

Figure 3.19 – Relationship between Speckle-Decorrelation and Calculated Perfusion when imaging one-cycle excitation and 16 bits Golay plane wave imaging when no noise is added.

The fact that the relationship is not perfectly linear can be explained by the fact that the datasets were not large enough (only 250 frames were acquired for a frame rate of 500 frames per second) to achieve SVD filter full potential and it was due to computational constraints.

The effect of noise on speckle-decorrelation rate calculation can be seen in Figure 3.20. When Golay sequences were used to calculate speckle decorrelation rates, even though different than when no noise was present, the values were consistent for different SNR proving the robustness of the proposed method. While the speckle-decorrelation calculated from data acquired using one cycle varied significantly for different SNR. Therefore, this validates that the use of Golay Sequences improves perfusion sensitivity.

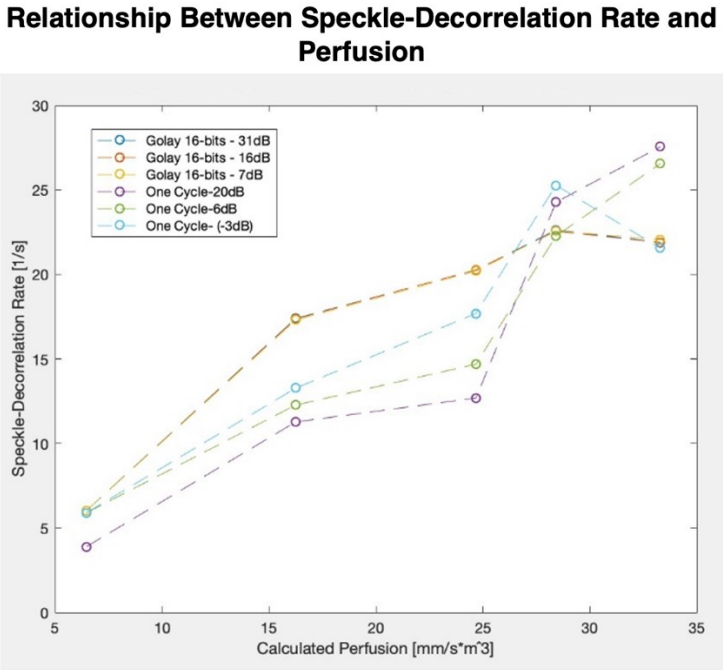

Figure 3.20 – Relationship between Speckle-Decorrelation and Perfusion when noise is added.

It is valid to notice that for speckle- decorrelation rates related to Golay Codes, a decrease in the speckle-decorrelation rate is seen when scatterers are moving at 5mm/s. This is due to the fact that we need to assume that the medium is not moving to perform pulse compression, however, the particles are moving too fast and this hypothesis does not hold. Therefore, the estimated speckle-decorrelation rate is compromised.

Nevertheless, such high flow speeds are not the interest of this research whereas blood flow speed in the microvasculature is in the order of 0.1 to 1.5mm/s. Hence, the decision was made to implement Golay Codes on the Verasonics Vantage programmable ultrasound system to increase the perfusion sensitivity for *in vivo* experiments.

3.5 Limitations of Power Doppler on Perfusion Estimation

In Chapter 1 it was also hypothesized that Power Doppler, even though being a powerful tool on estimating blood flow, is not able to quantitatively estimate perfusion which adds to the novelty of this method. As can be seen in Figure 3.21, there is no difference in mean power of the signal when scatterers are moving at 1mm/s or 5mm/s.

Power Doppler played an important role on identifying regions where blood was flowing and was used as a mask on the automation of the presented method. The algorithm here implemented does not require a physician or technician to identify the region of interest where the blood is flowing since it is done automatically.

However, the proposed method to estimate tissue perfusion by calculating the speckle-decorrelation rate is superior to the Power Doppler imaging because it provides quantitative information and not only information on the morphology. Furthermore, the proposed method is also superior to the perfusion estimation proposed by Choi *et al.* [59] which is compression-based and uses photoacoustic signals. In the latter, it is possible to obtain quantitative information on tissue perfusion, but not information on the morphology since PA signals are spatially unresolvable.

This study provides a method to provide simultaneously quantitative and morphologic information on tissue perfusion.

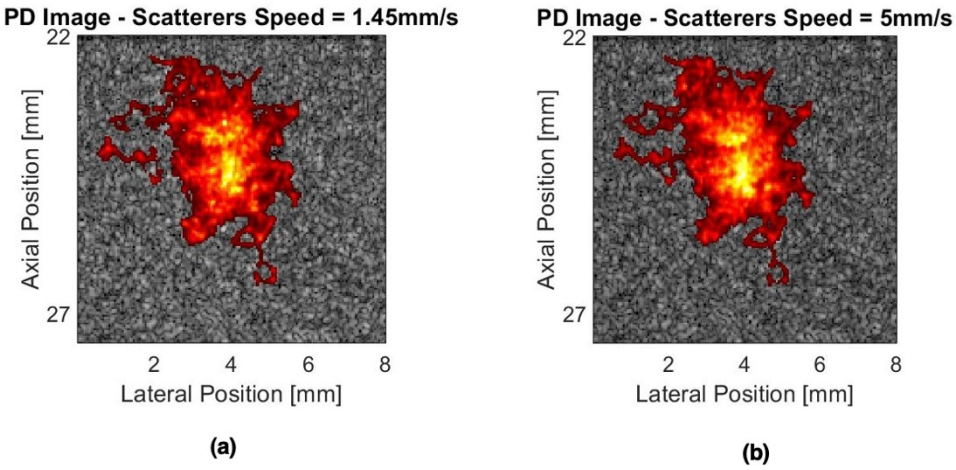

Figure 3.21 – Power Doppler images (a) for scatterers moving at 5mm/s and (b)for scatterers moving at 1mm/s.

Chapter 4

Experiments

4.1 Introduction

Even though simulations were a great tool in developing and fine tunning the method proposed by this study, the necessity of proving that speckle decorrelation rate is proportional to tissue perfusion for *in vivo* experiments was critical to ensure that this method can be used in clinical applications in the future.

Therefore, a relatively simple experiment was proposed that could be replicated several times to provide enough data to statistically analyze the population. The experiment in question involves submerging the subject's hand in cold water (to decrease perfusion) and in hot water (to increase perfusion).

4.2 Perfusion of the Palm

4.2.1 Hot and Cold Water Experiments

Initial *in vivo* study was conducted by imaging the hand of a human subject. The experiments were performed using Visualsonics LZ250 21MHz linear array transducer connected to a Verasonics Vantage programmable ultrasound system. We used plane wave compounding imaging with seven different angles at a frame rate of 500 frames per second.

The hand of the human subject was submerged in either hot (45°C) or cold (12°C) water baths for 45 seconds. The hot water enhanced perfusion while the cold water decreased it. The system setup can be shown on Figure 4.1.

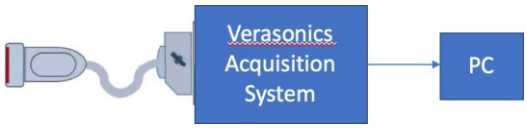

Figure 4.1 – System setup for acquiring US images.

The results can be shown on Figures 4.2 where for different data acquisitions the perfusion mapping for like temperatures is similar which validates the proposed method. Moreover, as one would expect, the speckle decorrelation rate increased when the subject's hand was submerged in hot water.

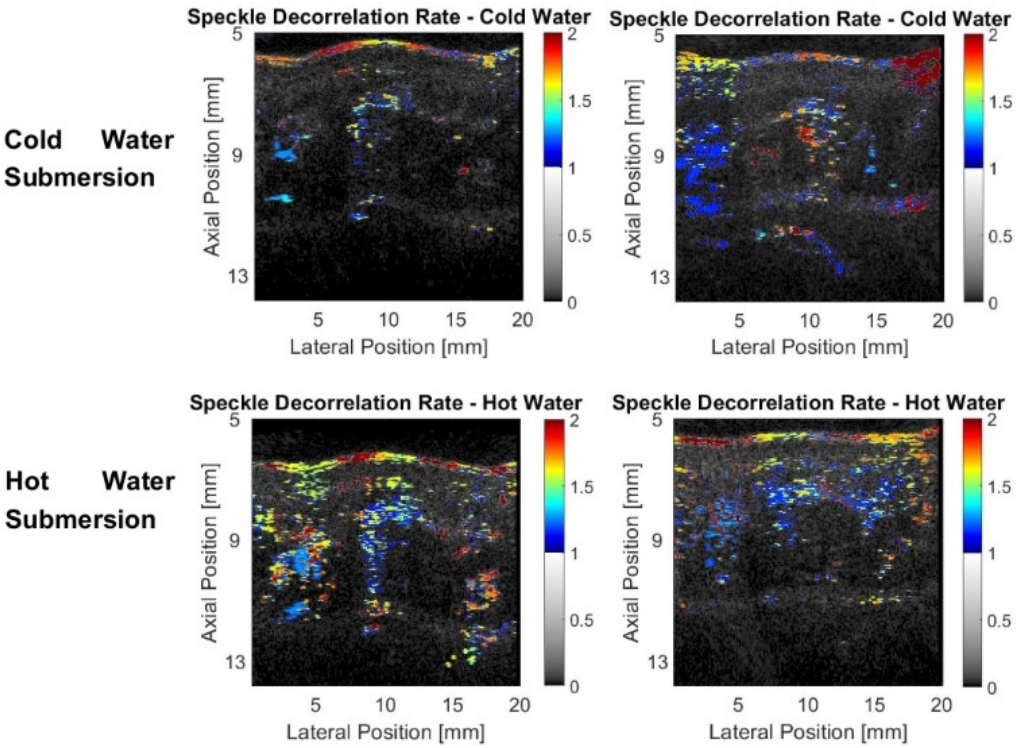

Figure 4.2 – Perfusion mapping generated by imaging the speckle decorrelation rate for cold and hot water submersion. Gray colormap represents the normalized backscattered signal and the overlay represents the normalized speckle-decorrelation rate.

Figure 4.3 shows the mean speckle decorrelation rate for the different datasets which the perfusion mapping is shown in Figure 4.2. It is possible to see a considerable high standard deviation that can be explained by the fact that perfusion would change faster on the superficial layer of the skin and the same change is not seen deeper in the tissue.

Furthermore, we performed a t-test on the data acquired at the same temperature and were able to conclude that similar datasets came from the same data population with a 5% confidence.

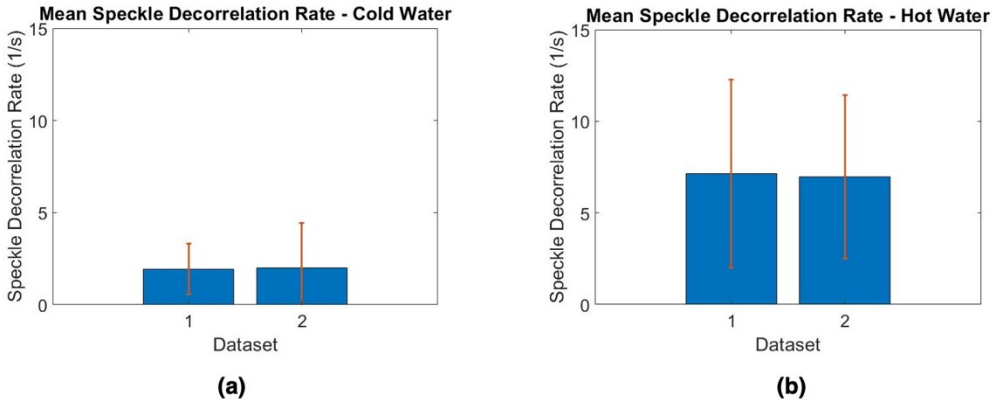

Figure 4.3 – Mean speckle decorrelation rate for different datasets acquired at the same temperatures (a) mean speckle decorrelation rate for cold water submersion (b) mean speckle decorrelation for hot water submersion.

Initial *in vivo* experiment results were promising. However, not all data acquired could be considered good data since transducer movements was being interpreted by the proposed algorithm as change in tissue perfusion. In addition, the subject had to stay still which is not always the case in clinical applications.

To address the clutter motion (also responsible for the high standard deviation), we used the AM2D algorithm to track tissue motion and analyse the correlation of the same speckles frame by frame. Moreover, we use the adaptive block-wise SVD filter to also increase perfusion sensitivity.

This increased the robustness of the proposed method as shown on Figure 4.4. For the same dataset (that was not considered “good data” previously due to considerable clutter motion) we were able to improve the sensitivity of the perfusion estimation data by combining the AM2D algorithm and the adaptive block-wise SVD filter.

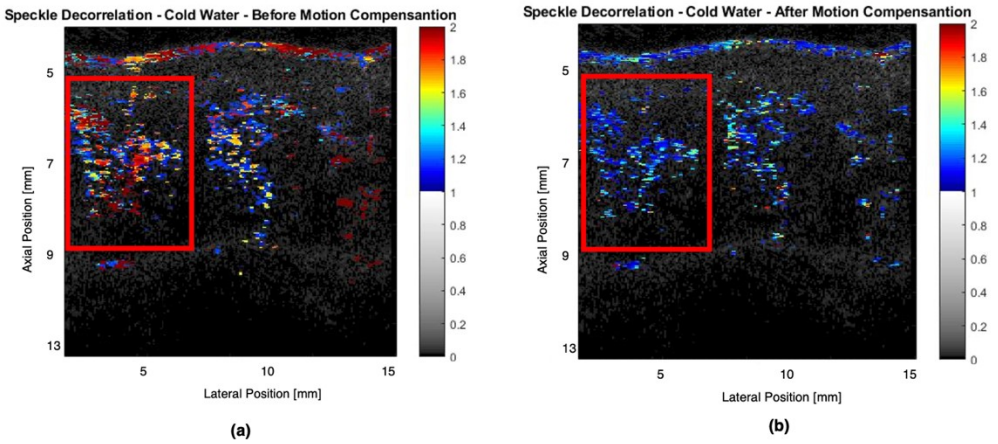

Figure 4.4 – Perfusion sensitivity increased after using the AM2D algorithm and the adaptive block-wise SVD filter on the same dataset (a) AM2D is absent (b) AM2D was implemented. Gray colormap represents the normalized backscattered signal and the overlay represents the normalized speckle-decorrelation rate.

Even after implementing the adaptive block-wise SVD filter the system noise was still an issue and we used Golay sequences to improve the sensitivity of our method. Due to setup constraints we investigated the use of a different transducer (Philips L7-4) that has a much lower central frequency but provided us the capability of seeing live PD images which made it easier to image the same region of the palm and assuring the same population was being considered. Our first hypothesis was that lower frequency transducer would not be sensitive to blood flow in microvasculature given the lower resolution. However, the combination of the AM2D algorithm on the RF data combined with the use of block-wise SVD filter with adaptive threshold on the reconstructed data proved to isolate the blood signal very well to the point a lower frequency transducer could be used. The results are shown on Figure 4.5.

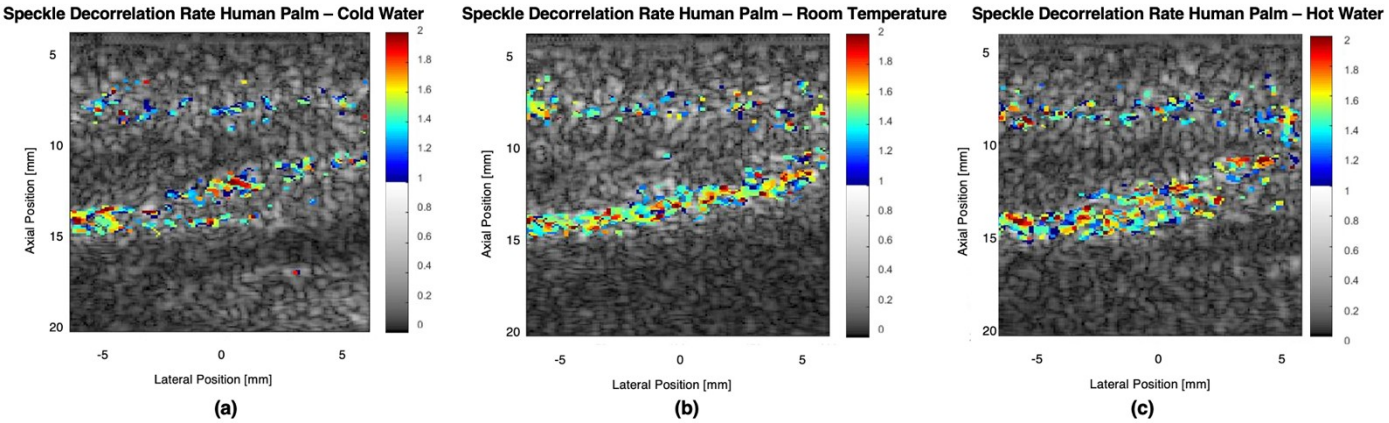

Figure 4.5 – Speckle-decorrelation rate for images acquired with the lower frequency transducer (a) cold water submersion (b) room temperature submersion (c) hot water submersion. Gray colormap represents the normalized backscattered signal and the overlay represents the normalized speckle-decorrelation rate.

Figure 4.6 shows a statistical analysis for the data acquired using the lower frequency transducer when 10 datasets were acquired for each temperature. For the cold water the mean speckle-decorrelation rate was 5.47 (1/s) and the standard deviation was found to be 3.49 (1/s). For the room temperature the mean speckle-decorrelation rate was 24.06 (1/s) and the standard deviation was found to be 8.57 (1/s). For the hot water the mean speckle-decorrelation rate was 42.08 (1/s) and the standard deviation was found to be 15.79 (1/s). A t-test was performed on the datasets acquired at the same temperature and a 5% level of confidence that the data comes from the same population was achieved.

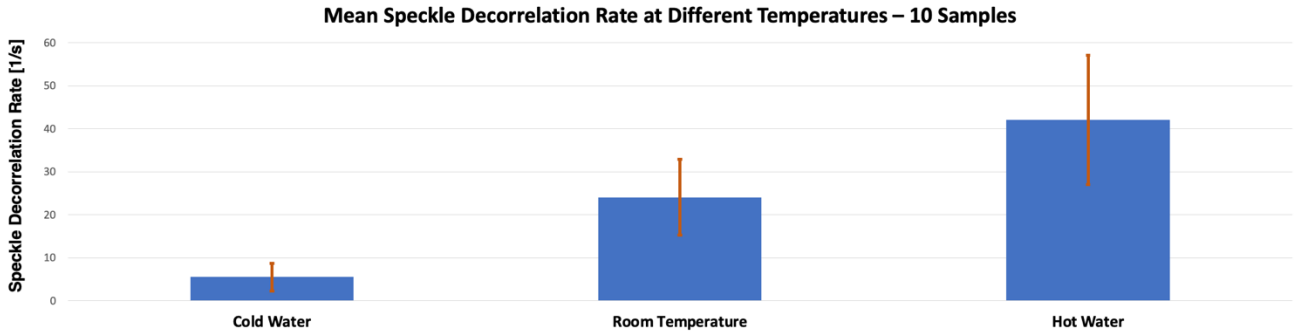

Figure 4.6 – Mean speckle decorrelation rate when using the lower frequency transducer.

We expanded the experiment to use the high-frequency transducer after implementing the Golay sequences code to be used in the Verasonics system. Figure 4.7 shows the perfusion mapping at different temperatures when the Visualsonics LZ250 21MHz linear array transducer was used.

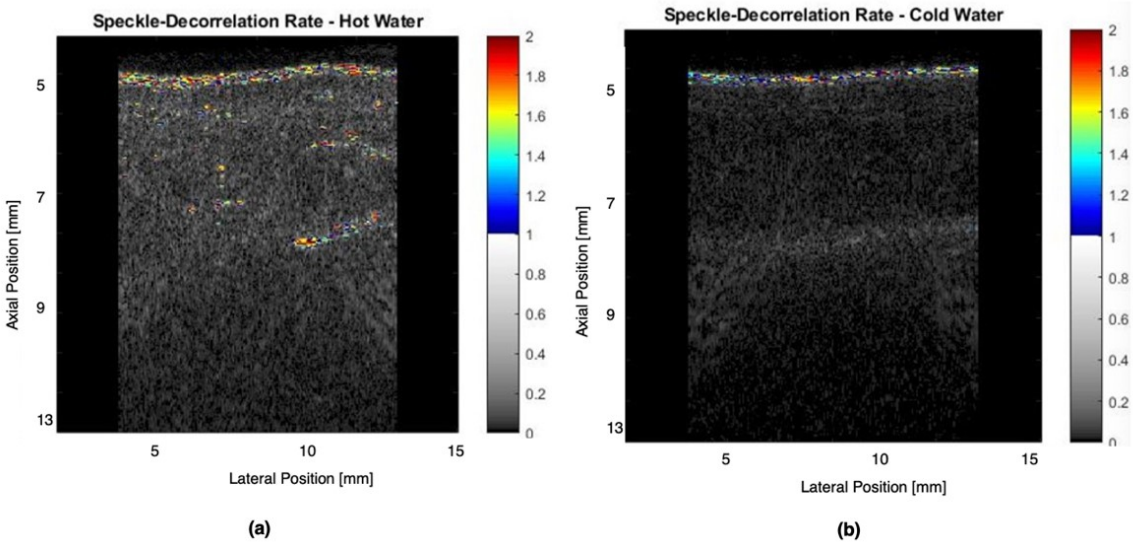

Figure 4.7 – Speckle-Decorrelation Rate of human palm at different temperatures when 16-bit Golay sequences were used to acquire the data. Gray colormap represents the normalized backscattered signal and the overlay represents the normalized speckle-decorrelation rate.

Moreover, Figure 4.8 shows the perfusion mapping (for data roughly at same location) when only one cycle was used, and it is possible to notice weaker signals even when perfusion should be enhanced in the hot water bath. It is valid to notice that all post-processing methods were the same, including the block-wise SVD filter and the use of the AM2D algorithm.

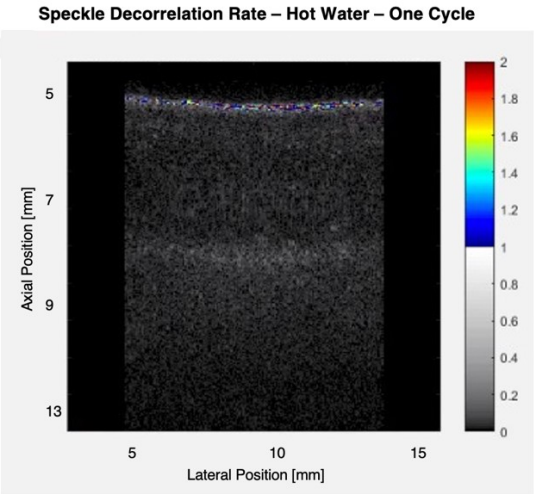

Figure 4.8 – Speckle decorrelation rate of human palm when one cycle plane wave compounding imaging was used. Gray colormap represents the normalized backscattered signal and the overlay represents the normalized speckle-decorrelation rate.

However, when using Golay sequences, as was indicated by simulation results, one needs to be careful about scatterers moving at higher speeds since in order we assume that the medium in not moving between two insonifications as mentioned in Chapter 3.

We also analyzed the effect of the frame rate when using Golay sequences and, as shown on Figure 4.9, it is noticeable that for a lower frame-rate the speckle-decorrelation rate is compromised for scatterers moving at lower speeds, in this case at 4mm/s. This leads us to hypothesize that increasing the frame rate would allow the creation of perfusion mapping images when the blood flow is higher. Further studies need to be done to confirm this hypothesis. It is evident that the change in framerate also impacts the value of the speckle decorrelation rate and this relationship must be investigated further and be weigh in when providing perfusion values that can be used in clinical applications.

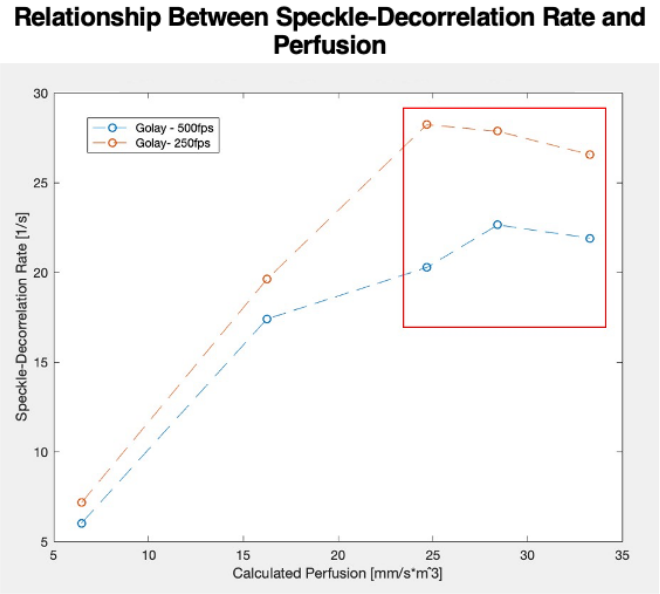

Figure 4.9 – Speckle-decorrelation rate being compromised by scatterers speed and the effect of the frame-rate.

The hypothesis that speckle-decorrelation rate relates to tissue perfusion were confirmed by this study. Moreover, we validated that a combination of block-wise SVD filter, AM2D algorithm for tissue motion compensation and the use of Golay sequences significantly increase perfusion sensitivity.

4.3 Photoacoustic Data

4.3.1 Estimation of Oxygen Saturation in Phantom

Combining the proposed method to estimate tissue perfusion, which shows great potential to estimating blood flow speed, with PA signals that can be used

to estimate sO2 as described on Section 2.5.1 can lead to estimating blood oxygen saturation and rate of oxygen consumption, two parameters that are extremely important when studying tissue metabolism and diseases related to oxygen metabolism.

We performed a simple experiment that allowed us to estimate blood oxygen saturation as well as blood flow speed. To accomplish that we used a tunable optical parametric oscillator (Surelite OPO Plus, Continuum, CA, USA) that was pumped by a Q-Switch Nd: YAG nanosecond-pulsed laser (Surelite III, Continuum, CA, USA) at repetition rate of 10Hz. The laser beam passed through a lens in order to focus it to a fiber bundle light-guide, and it was also split in order to be detected by a photodiode (Thorlabs, DET100A/M) the fiber bundle is connected to a linear array ultrasound transducer LZ250 (FUJIFILM, VisualSonics, Inc.). A Verasonics Vantage 256 (Verasonics, Inc., Remon, WA, USA) ultrasound acquisition system was used in conjunction with this transducer. The computer was responsible for triggering the Q-Switch, and the raw data collected was postprocessed using MATLAB (The MathWorks, Inc., Natick, MA, usa). Figure 4.10 shows the schematic of the constructed system used on the *in vivo* experiments.

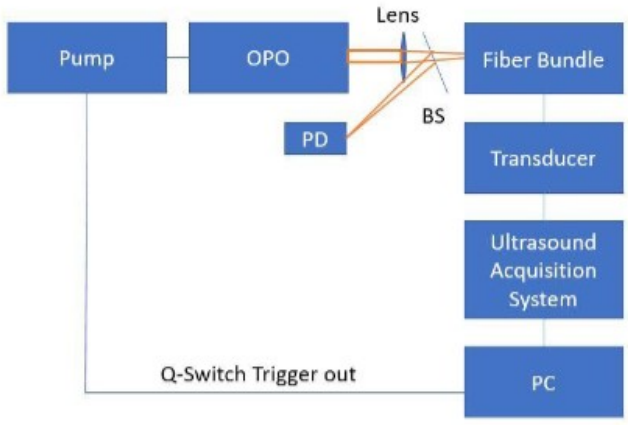

Figure 4.10 – Schematic of light deliver and data acquisition setup.

An appropriate software was used to tune the excitation wavelength, and a wavelength calibration system (Ocean Optics USB400) was used to determine the precise excitation wavelength.

In order to estimate blood oxygen saturation, PA signals were obtained using wavelengths between 705nm and 820nm, which are in the transparent window range, where optical fluence varies slowly. In one set of data (non-scattering phantom) three wavelengths were used: 705nm, 750nm and 810nm. While for the scattering phantom, PA signals were acquired using seven different wavelengths: 705nm, 720nm, 740nm, 760nm, 780nm, 800nm, and 820nm.

The setup for the in vitro experiment is shown on Figure 4.11. The same setup was used to acquire the PA data and the high frequency ultrasound data, which was used to estimate blood flow. In the schematic the ultrasound transducer is right on top of the sample for water coupling.

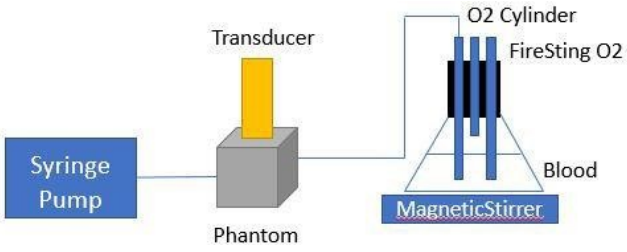

Figure 4.11 – Setup for in vitro experiment using rat blood.

To have control of the oxygenation level the sensor FireStingO2 (PyroScience, Aachen, Germany) was used. The sensor was calibrated using nitrogen until the measured oxygen level was close to zero.

The FireStingO2 was placed in the task with a four-hole stopper and filled with rat blood, which was also connected through a tube to the oxygen cylinder. To change the oxygenation level inside the task, the O_2 cylinder was open, while the blood was being stirred by the magnetic stirrer. When the oxygen level was

close to the desired preset value, the oxygen cylinder was closed, the magnetic stirrer turned off and blood was withdrawn to the vessel inside the phantom. This process was repeated many times in order to get oxygen levels varying from 20% to 80%. Moreover, for each preset level a different set of data was obtained for each wavelength.

To acquire the blood flow data we used a syringe pump. Speed rates were calculated based on the diameter of the tube in the phantom, and on the desired speed flow. Speed flows of 0.1mm/s, 0.3mm/s, 0.5mm/s, 0.7mm/s, 1mm/s and 5mm/s were used to acquire data using the high-frequency ultrasound (US) transducer with central frequency at 21MHz.

The experiments were performed on flow phantom. Transparent polyurethane tubing (SAI Infusion Technologies, IL, USA) with inner diameter (ID) of 1.016mm was used to mimic a blood vessel. One vessel was embedded at 5mm deep inside a phantom. A non-scattering phantom with 10% gelatin by mass as well as a tissue mimicking phantom composed of 10% gelatin and 10% cornstarch by mass (this composition provides ultrasonic and mechanical properties similar to human tissue) were used.

The ultrasound transducer was responsible for delivering the laser beam and acquiring the acoustic waves generated by the photoacoustic effect.

PA images of the cross-sectional view of the vessel were obtained when there was no blood flow. Preset values of sO_2 varying from 3% to 80% for the non-scattering phantom, and 20% to 80% for the scattering phantom were used. For each preset sO2 100 PA images were taken for each wavelength. The photodiode was used for laser-pulse normalization. The 100 normalized PA images related to one wavelength were averaged.

Blood flow data was acquired at a constant oxygenation level and flow speed varying from 0.1mm/s to 5mm/s were evaluated for frame rates of 100Hz, 250Hz, and 500Hz using plane wave imaging.

Figure 4.12 shows the measured sO_2 for the scattering phantom. The maximum error between measured sO_2 and the preset values was around 16.8%

(sO2 equals to 50%) while the minimum error was 1.21% for a preset sO_2 equaling 90%. The linear regression indicates a relationship with a correlation coefficient $R^2 = 0.85$.

Using the proposed speckle-decorrelation method and comparing with the values set at the pump we were able to estimate the velocity (Figure 4.12) which is another important parameter on estimating sO_2.

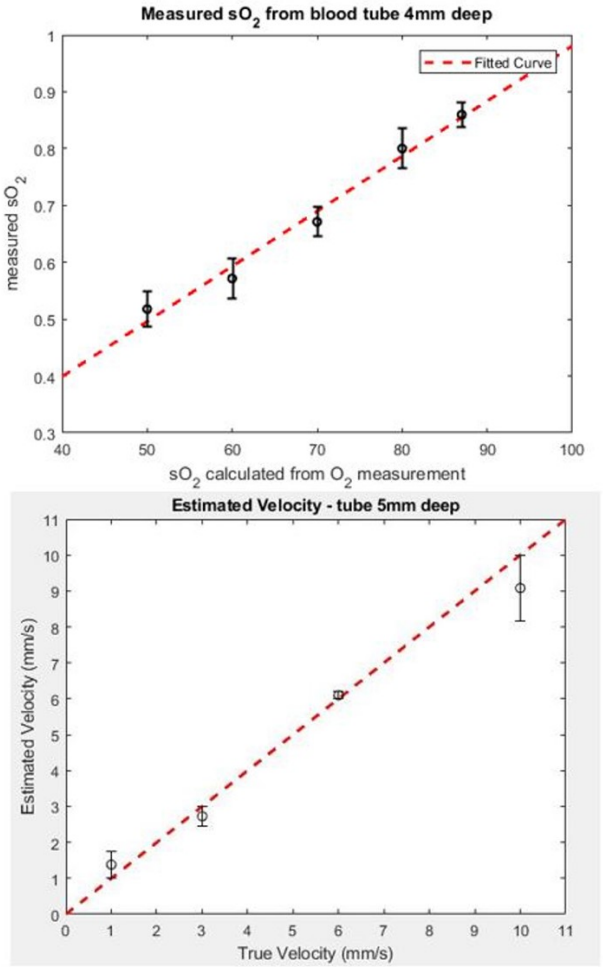

Figure 4.12 – Estimated sO2 (from peak amplitude PA signal) vs. Preset sO2. Estimated Velocity (from ultrafast speckle decorrelation method) vs. True Velocity.

In a single vessel the rate of oxygen consumption is estimated based on three parameters: cross-section area of the vessel, sO_2 and the mean flow speed. The estimated velocity shown in Figure 4.12 was calculated based on Equation 3.5 and the remaining cross-section parameter can be calculated using the PD image of the cross-section of the tube. Figure 4.13 shows that PD imaging outperforms PA imaging in providing cross-section information.

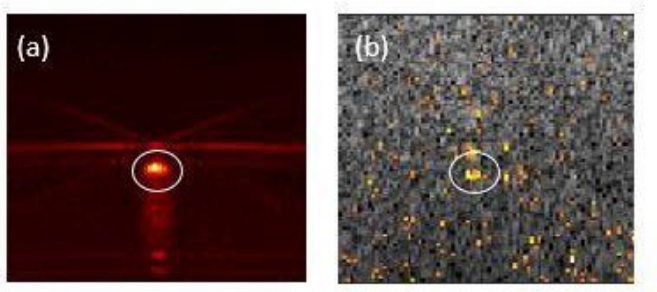

Figure 4.13 – (a) normalized Power Doppler image (b) Normalized PA image overlaid on B-scan ultrasound image.

The method proposed here to estimate velocity makes use of a linear array ultrasound transducer instead of the single element transducer that is usually used for this purpose. Several advantages are related to this including no need for mechanical scanning and the lack of moveable parts makes it less hazardous to patients.

During the cold and hot water experiments we also analyzed the photoacoustic data. We used deep PAM to estimate oxygen saturation by using photoacoustic signals at 7 different wavelengths (680 to 800nm).

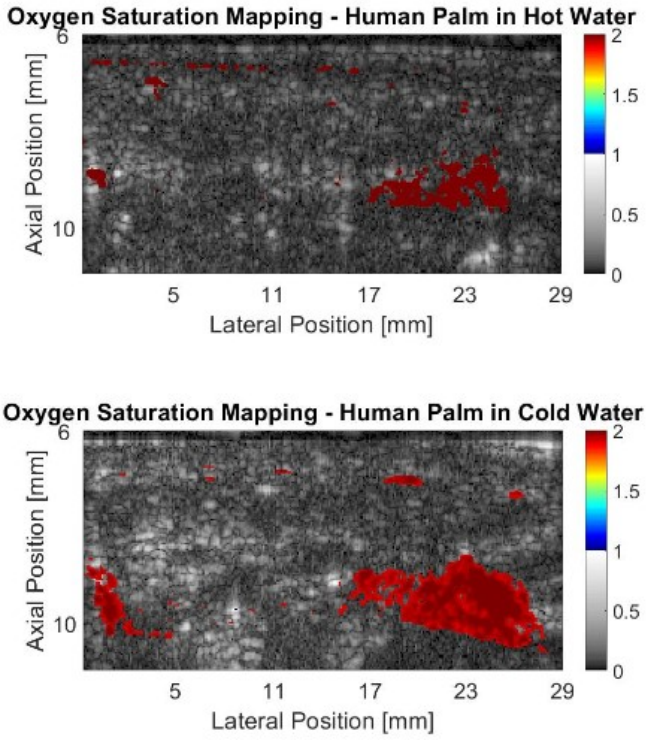

Figure 4.14 – Oxygen saturation estimation using 7 wavelengths (a) hot water submersion (b) cold water submersion. Gray colormap represents the normalized backscattered signal and the overlay represents the normalized PA signal.

We found no statistically-significant difference in sO_2 observed between hot and cold-water as one would expect. Moreover, similarly to what happens in capillaries where small diameters makes it a challenge to estimate blood flow, and therefore, the tissue perfusion defined as the blood volume provided to a unit volume of tissue per second becomes the parameter of interest to assess microvascular beds, to estimate MRO_2 in the microvasculature one can rely on tissue perfusion and sO_2 quantification alone (waving the need to assess cross-section area and velocity separately). Consequently, the method proposed in this study that uses speckle decorrelation rate to estimate tissue perfusion is a strong option to be used in the future to estimate rate of oxygen consumption.

However, to fully estimate MRO_2 one needs to account for the oxygen carried by RBCs and by the plasma. The amount of oxygen carried by plasma or hemoglobin depends on the pressure of oxygen (pO_2), but since the solubility of oxygen in plasma is limited, most of the oxygen carried by hemoglobin can be calculated using the following formula [29]:

$$\rho_{O_2,Hb} = \zeta * C_{Hb} * sO_2 \quad (4.1)$$

Where ζ is the oxygen-binding capacity to Hb, which previous studies found to be 1.34ml/gHb when the hemoglobin is completely saturated by oxygen, and C_{Hb} and sO_2 can be estimated using multiwavelength photoacoustic methods [29]. Also, the oxygen carried in the plasma can be calculated using the following:

$$\rho_{O_2,plasma} = \alpha_{O_2}(T) * pO_2 \quad (4.2)$$

Where α_{O2} is the solubility of oxygen in plasma as a function of temperature. Therefore, estimating pO_2 is also important to provide accurate estimation of oxygen flux.

There is still a long way in combining the proposed speckle-decorrelation method and photoacoustic data to fully estimate oxygen saturation. However, initial results are promising adding to the great benefits the proposed method can bring to the clinical domain including tissue perfusion estimation and estimation of higher blood flow speeds when the proper framerate is chosen.

Chapter 5

Conclusion

There is great relevancy in estimating tissue perfusion and the clinical applications are several, including assessment of peripheral vascular disease, management of diabetic feet and limbs, management of angiogenic therapies, stroke management and assessment of transplanted organs.

Ultrasound perfusion imaging is preferable to other non-invasive methods (SPECT, CT, MRI, PET, etc.) since it is relatively inexpensive. Two main ultrasound imaging techniques are currently used in estimating perfusion: power Doppler and contrast-enhanced ultrasound.

Nevertheless, the use of contrast agents is not approved by FDA for several applications and mostly CEUS still depends on Doppler shift to estimate blood flow and therefore microbubbles must be flowing at speeds higher than the ones found in capillary beds. Furthermore, PD imaging combined with advanced clutter filtering techniques significantly increased perfusion sensitivity, but only provides information about the morphology and not necessarily quantitative perfusion information provided by CEUS.

This study bridged the gap between PD imaging and CEUS by using speckle-tracking techniques to provide both morphological and quantitative perfusion information. Moreover, the proposed method also outperforms the non-invasive method proposed by Choi *et al.*, [59] that provides quantitative perfusion information, but lacks morphological information since PA signals are non-resolvable.

Still, previous research around tissue motion compensation for use with CEUS and the method proposed by Choi *et al.* were of great value for this research since suppressing tissue signal is a great challenge when imaging microvascular beds and estimating tissue perfusion. Furthermore, the advancements in PD

imaging when complex clutter filters are used allowed us to use the PD data as a mask to isolate the microvasculature (to subsequently calculate the speckle decorrelation rate) to minimize the need for doctors and technicians to specify a ROI.

We validated that the use of PWC combined with adaptive block-wise SVD filter increases perfusion sensitivity to a level where reliable speckle decorrelation rates can be calculated. However, we did not pursue calculating the speckle decorrelation for the case when scan-line acquisition and the HOSVD filter proposed by Kim *et al.* [21] is used which similarly could lead to great speckle decorrelation estimation.

We successfully proved that perfusion rate is proportional to the speckle-decorrelation rate calculated as the reciprocal of the standard deviation of the Gaussian curve fitted to the autocorrelation function in time. The same Gaussian curve can also lead to estimating flow velocity when the lateral width of the received point spread function (PSF) is known for plane wave acquisition.

The hypothesis that speckle-decorrelation rate is proportional to tissue perfusion was proven by implementing realistic 2D and 3D random walk microvasculature simulations that were based on hemodynamics theory to assure speckles were moving similarly to RBCs and parameters such as change in pressure and flow from parent nodes to daughter nodes were considered.

Nonetheless, despite the great progress and foundation laid by the use of simulations, *in vivo* experiments exposed the need of a tissue motion compensation technique to account for axial and lateral displacements of tissue when clutter signal has the same order of magnitude as blood signal. To address this issue, we used the AM2D algorithm that increased sensitivity. However, this algorithm relies on RF data that is not always provided by ultrasound manufacturers and the conversion of log compressed signals can decrease the efficacy of the algorithm.

The use of the adaptive block-wise SVD filter also increased perfusion sensitivity while maintaining the spatial resolution that had been compromised

by spatially averaging the data when 2nd order SVD filter was used. However, the block-wise SVD filter considered noise to be Gaussian, which is not necessarily true in most *in vivo* applications.

Therefore, we used Golay codes to increase SNR and consequently perfusion sensitivity. When 16 codes were used the SNR was increased by 15dB.

We first had hypothesized that we could only use high-frequency ultrasound transducers to estimate tissue perfusion since blood is more echogenic than tissue at higher frequencies. Nevertheless, the combination of the adaptive block-wise SVD filter, AM2D algorithm for tissue motion compensation and Golay codes, significantly improved SNR to the point that a transducer with central frequency of 7MHz was used to successfully estimate tissue perfusion *in vivo*. However, spatial resolution was still lacking.

We initiated the effort to estimate MRO2 with experiments in phantoms, and were able to estimate sO2, flow velocity and the cross-section are of one vessel which are the 3 main parameters used for estimating MRO_2 in one vessel. Furthermore, estimating sO_2 *in vivo* at different temperatures showed no statistically significant difference as one would expect and combining such information with the proposed method to estimate perfusion based on speckle decorrelation can lead to estimating oxygen metabolism in the microvasculature. However, more experiments and research must be done to fully estimate MRO2 *in vivo*.

In conclusion, the use of high-frequency high-frame rate ultrasound shows promise for estimating tissue perfusion rates without contrast agents. The hypothesis that speckle-decorrelation rate relates to tissue perfusion was confirmed in this study. To ensure the robustness of the method *in vivo* and focusing on future clinical applications we used of the adaptive block-wise SVD filter, the AM2D algorithm for tissue compensation and Golay sequences to significantly increase perfusion sensitivity to the point diagnostic lower frequency transducers could be used in perfusion estimation.

Future studies are needed to calibrate speckle-decorrelation rate with the framerate to provide people in the medical field with the proper perfusion values. In addition, there is still a long way in combining perfusion estimation with blood oxygen saturation to estimate oxygen metabolism, but initial findings are promising.

Bibliography

1. Quaia, Emilio, "Assessment of tissue perfusion by contrast-enhanced ultrasound," European Radiology 21.3, 604-615 (2011).

2. Feingold, Steven *et al.,* "Quantitative volumetric perfusion mapping of the microvasculature using contrast ultrasound," Investigative radiology 45.10 (2010).

3. Bruce, Matthew *et al.*, "Vascular flow and perfusion imaging with ultrasound contrast agents, " Ultrasound in medicine & biology 30.6, 735-743 (2004).

4. Hoyt, Kenneth *et al.*, "Ultrasound imaging of breast tumour perfusion and neovascular morphology," Ultrasound in medicine & biology 41.9, 2282-2302 (2015).

5. Chomas, James *et al.,* "Subharmonic phase-inversion for tumor perfusion," IEEE Ultrasonics Symposium. Proceedings. An International Symposium (Cat. No. 01CH37263). Vol. 2, IEEE (2001).

6. Melz, M., *et al.*, "Quantitative ultrsound perfusion analysis in vitro," Proceedings of Biosignal (2010).

7. Sridharan, Anush *et al., "*Perfusion estimation using contrast enhanced three-dimensional subharmonic ultrasound imaging: an in vivo study," Investigative radiology, 48.9, 654 (2013).

8. Tsui, Po-Hsiang, Chih-Kuang Yeh, and Chien-Cheng Chang. "Microvascular flow estimation by microbubble-assisted Nakagami imaging," Ultrasound in medicine & biology, 35.4, 653-671 (2009).

9. Jansson, T., H. W. Persson, and K. Lindstrom, "Estimation of blood perfusion using ultrasound," Proceedings of the Institution of Mechanical Engineers, Part H: Journal of Engineering in Medicine 213.2, 91-106 (1999).

10. Fosberg, Flemming *et al.,* "In vivo perfusion estimation using subharmonic contrast microbubble signals," Journal of ultrasound in medicine 25.1, 15-21 (2006).

11. Thijssen, Johan M., and Chris L. de Korte, "Modeling ultrasound contrast measurement of blood flow and perfusion in biological tissue," Ultrasound in medicine & biology 31.2, 653-671 (2009).

12. Arditi, Marcel *et al.,* "A new formalism for the quantification of tissue perfusion by the destruction-replenishment method in contrast-enhanced ultrasound," European radiology 21.3, 604-615 (2011).

13. Wei, Kevin *et al.,* "Quantification of myocardial blood flow with ultrasound-induced destruction of microbubbles administered as a contrast venous infusion," Circulation 97.5, 473-483 (1998).

14. Tsui, Po-Hsiang, Chih-Kuang Yeh, and Chien-Cheng Chang, "Microvascular flow estimation by contrast-assisted ultrasound B-scan and statistical parametric images," IEEE Transactions on Information Technology in Biomedicine 13.3, 360-369 (2009).

15. Mule, Sebastien *et al.,* "An original methodology for quantitative assessment of perfusion in small animals studies using contrast-enhanced ultrasound," 29th Annual International Conference of the IEEE Engineering in Medicine and Biology Society. IEEE (2007).

16. Rognin, Nicolas *et al.,* "A new approach for automatic motion compensation for improved estimation of perfusion quantification parameters in ultrasound imaging," 8th French Conference on Acoustics (2006).

17. Rognin, Nicolas G. *et al.,* "In vivo perfusion quantification by contrast ultrasound: Validation of the use of linearized video data vs. raw RF data," IEEE Ultrasonics Symposium (2008).

18. Lamuraglia, Michele *et al.,* "Clinical relevance of contrast-enhanced ultrasound in monitoring anti-angiogenic therapy of cancer: current status and perspectives," Critical reviews in oncology/hematology 73.3, 202-212 (2012).

19. Dymling, Stephan O., Hans W. Persson, and C. Hellmuth Hertz, "Measurement if blood perfusion in tissue using Doppler ultrasound," Ultrasound in medicine & biology 17.5, 433-444 (1991).

20. Kim, MinWoo *et al.*, "Expanding acquisition and clutter filter dimensions for improved perfusion sensitivity," IEEE transactions on ultrasounds, ferroelectrics, and frequency control 64.10, 1429-1438 (2017).

21. Kim, MinWoo *et al.,* "Multidimensional Clutter Filter Optimization for Ultrasonic Perfusion Imaging," IEEE transactions on ultranocis and ferroelectrics, and frequency control 65.11, 2010-2029 (2018).

22. Demene, Charlie *et al.,* "Spatiotemporal clutter filtering of ultrafast ultrasound data highly increases Doppler and fUltrasound sensitivity," IEEE transactions on medical imaging 34.11, 2271-2285 (2015).

23. Song, Pengfei *et al.,* "Ultrasound small vessel imaging with block-wise adaptive local clutter filtering," IEEE transactions on medical imaging 36.1, 251-262 (2017).

24. Tierney, Jaime, Don Wilkes, and Brett Byram, "Adaptive Independent Component Analysis-Based Clutter Filtering For Improved Non-Contrast Perfusion Ultrasound Imaging," IEEE International Ultrasonics Symposium, IEEE (2018).

25. Adler, Ronald S. *et al.,* "Ultrasonic estimation of tissue perfusion: a stochastic approach," Ultrasound in medicine & biology 21.4, 493-500 (1995).

26. Jirik, Radovan *et al.,* "Ultrasound perfusion analysis combining bolus-tracking and burst-replenishment," IEEE transactions on ultrasonics, ferroelectrics, and frequency control 60.2, 310-319 (2013).

27. Zeitz, Oliver *et al.,* "Estimation of choroid perfusion by colour Doppler imaging vs. other methods," Ultrasound in medicine & biology 28.8, 1023-1027 (2002).

28. Bohs, L. N. *et al.,* "Speckle-tracking for multidimensional flow estimation," Ultrasonics 38.1-8, 369-375 (2000).

29. Jiang, Y. *et al.*, "Blood Oxygen flux estimation with a combined photoacoustic and high-frequency ultrasound microscopy system: a phantom study," Journal of Biomedical Optics 17, (2012).

30. Jiang, Y. *et al.,* "Estimation of cerebral metabolic rate of oxygen consumption using combined multiwavelength photoacoustic microscopy and Doppler microultrasound," Journal of Biomedical Optics 23, (2018).

31. Xia, J. *et al.,* "Calibration-free quantification of absolute oxygen saturation based on the dynamics of photoacoustic signals," Opt Letters 38, (2013).

32. Perekatova, V. *et al.,* "Optimal wavelengths of optoacoustic measurements of blood oxygen saturation in biological tissues," Biomedical Optics Express 7, (2016).

33. Cao, F. *et al.,* "Photoacoustic imaging in Oxygen Detection", Applied Sciences 7, (2017).

34. Song, Khang Ho, Brandon K. Harvey and Mark A. Borden, "State of the Art Microbubble assisted blood brain barrier disruption," 8.16, 4393 (2018).

35. Chatuverdi, Devendra K. "Modeling and Simulation of Systems Ssing MATLAB" and Simulink. CRC press (2017).

36. Jensen, Jorgen Arendt. "Field: A Program for Simulating Ultrasound Systems". 10th Nordicbaltic Conference on Biomedical Imaging, Vol. 4, Supplement 1, Part 1: 351--353 (1996).

37. Jensen, Jorgen Arendt. "Simulation of Advanced Ultrasound Systems using Field II". 2004 2nd IEEE International Symposium on Biomedical Imaging: Nano to Macro. 636-639 IEEE (2004).

38. Bujoreanu, Denis, *et al.* "A Resolution Enhancement Technique for Ultrafast Coded Medical Ultrasound". 2018 26th European Signal Processing Conference (EUSIPCO). IEEE (2018).

39. Karshafian, Raffi, Peter N. Burns, and Mark R. Henkelman. "Transit time kinetics in ordered and disordered vascular trees". Physics in Medicine & Biology 48.19 (2003): 3225.

40. Lashkari, Bahman, Kaicheng Zhang and Andreas Madelis. "High-frame-rate Synthetic Aperture Ultrasound Imaging Using Mismatched Coded

Excitation Waveform Engineering: A Feasibility Study". IEEE Transactions on Ultrasonics, Ferroelectrics, and Frequency Control 63.6 (2016): 828-841.

41. Alexander Graham Bell. "On the Production and Reproduction of Sound by Light". American Journal of Science, (118):305-324 (1880).

42. Lihong V Wang and Song Hu. "Photoacoustic tomography: in vivo imaging from organelles to organs". Science, 335(6075): 1458 - 1462 (2012).

43. Lal, C., Leahy, MJ. "Go with the Flow: A Review of Methods and Advancements in Microvasculature Blood Flow Imaging". Microcirculation, 23(5): 345-63 (2013).

44. Brunker, J., and Beard, P. "Pulsed Photoacoustic Doppler Flowmetry Using Time-Domain Cross-Correlation: Accuracy, resolution and scalability". Journal of the Acoustical Society of America, 132(3): 1780-1791 (2012).

45. Gottrup, F. "Physiology and Measurement of Tissue Perfusion". Annales Chirurgiae et Gynaecologiae. Vol. 83. No 3 (1994).

46. Scholbach, Thomas, Elisa Girelli, and Jakob Scholbach. "Dynamic Tissue Perfusion Measurement: A Novel Tool in Follow-up of Renal Transplants". Transplantation 79.12 (2005).

47. Minghua Xu and Lihong V Wang. "Photoacoustic Imaging in Biomedicine ". Review of Scientific Instruments, 77(4) (2006).

48. Patriquin, H., M. Lafortune, D. S. Babcock, and M. Dauzat. "Power Doppler Sonography: Basic Principles and Clinical Applications in Children". Pediatric Radiology, Vol. 2, No. 2: 109-115 (1996).

49. Xu, X., L. Sun, JM. Cannata, JT. Yen, and KK. Shung. "High-frequency Ultrasound Doppler System for Biomedical Applications with a 30MHz Linear Array". Ultrasound Med. Biology, Vol. 34, No. 4: 638-646 (2008).

50. Evans, Kevin, Brandon Weiss, and Michael Knopp. "High-intensity Focused Ultrasound (hifu) for Specific Therapeutic Treatments: A Literature Review". Journal of Diagnostic Medical Sonography 23(6):319-327 (2007).

51. Cobbold, Richard SC. "Foundations of Biomedical Ultrasound". Oxford Press (2006).

52. Tanter, Michael, and Mathias Fink. "Ultrafast Imaging in Biomedical Ultrasound". IEEE Transactions on Ultrasonics, Ferroelectrics and Frequency Control, 61(1):102-119 (2014).

53. Bercoeff, J *et al.* "Ultrafast Compound Doppler Imaging Providing Full Blood Flow Characterization". IEEE Trans. Ultrasound, Ferroelectrics, Frequency Control, Vol. 58, No. 1: 134-147 (2011).

54. T. Reichl, J. Passenger, O. Acosta, and O. Salvado, "Ultrasound goes GPU: real-time simulation using CUDA", Vol. 726116 (2009).

55. Viti J., H.J. Vos, N. De Jong, F. Guidi, P. Tortoli, "Contrast Detection Efficacy for Plane vs. Focused Wave Transmission", IEEE International Ultrasonics Symposium (2014).

56. Sivaramakrishnan, M., *et al.* (2007). Limitations of quantitative photoacoustic measurements of blood oxygenation in small vessels. Physics in Medicine and Biology. 52(5):1349-61.

57. Hennen, S N., *et al.* (2015). Photoacoustic Tomography imaging and estimation of oxygen saturation of hemoglobin in ocular tissue of rabbits. Experimental Eye Research. 153-8. doi: 10.1016.

58. Yao, J., Wang, LV., (2014). Photoacoustic Brain Imaging: from microscopic to macroscopic scales. Neurophotonics, 1(1). pii: 1877516.

59. Choi, Min, AM James Shapiro, and Roger Zemp. "Tissue perfusion rate estimation with compression-based photoacoustic-ultrasound imaging." Journal of Biomedical Optics 23.1 (2018): 016010.

60. Rivaz, Hassan, *et al.* "Real-time regularized ultrasound elastography." IEEE transactions on medical imaging 30.4 (2010): 928-945.

61. Shung, K. Kirk. "High frequency ultrasonic imaging." Journal of medical ultrasound 17.1 (2009): 25-30.

62. Yao, Junjie, and Lihong V. Wang. "Sensitivity of photoacoustic microscopy." Photoacoustics 2.2 (2014): 87-101.

63. Rubin, Jonathan M., Theresa A. Tuthill, and J. Brian Fowlkes. "Volume flow measurement using Doppler and grey-scale decorrelation." Ultrasound in medicine & biology 27.1 (2001): 101-109.

64. Van den Berg, P. J., Khalid Daoudi, and Wiendelt Steenbergen. "Review of photoacoustic flow imaging: its current state and its promises." Photoacoustics 3.3 (2015): 89-99.

65. Lal, Cerine, and Martin J. Leahy. "An updated review of methods and advancements in microvascular blood flow imaging." Microcirculation 23.5 (2016): 345-363.

66. Foster, F. Stuart, *et al.* "Advances in ultrasound biomicroscopy." Ultrasound in medicine & biology 26.1 (2000): 1-27.

67. Draijer, Matthijs, *et al.* "Review of laser speckle contrast techniques for visualizing tissue perfusion." Lasers in medical science 24.4 (2009): 639-651.

68. Song, Wei, Wenzhong Liu, and Hao F. Zhang. "Laser-scanning Doppler photoacoustic microscopy based on temporal correlation." Applied physics letters 102.20 (2013): 203501.

69. Liang, Jinyang, *et al.* "Cross-correlation-based transverse flow measurements using optical resolution photoacoustic microscopy with a digital micromirror device." Journal of biomedical optics 18.9 (2013): 096004.

70. Chen, Sung-Liang, *et al.* "Photoacoustic correlation spectroscopy and its application to low-speed flow measurement." Optics letters 35.8 (2010): 1200-1202.

71. Chen, Sung-Liang, *et al.* "In vivo flow speed measurement of capillaries by photoacoustic correlation spectroscopy." Optics letters 36.20 (2011): 4017-4019.

72. Brunker, Joanna, and Paul Beard. "Acoustic resolution photoacoustic Doppler velocimetry in blood-mimicking fluids." Scientific reports 6.1 (2016): 1-16.

73. Chen, Sung-Liang, *et al.* "Photoacoustic correlation technique for low-speed flow measurement." Photons Plus Ultrasound: Imaging and Sensing 2010. Vol. 7564. SPIE, 2010.

74. Bücking, Thore M., *et al.* "Processing methods for photoacoustic Doppler flowmetry with a clinical ultrasound scanner." Journal of biomedical optics 23.2 (2018): 026009.

75. Zhang, Ruiying, *et al.* "Structured-illumination photoacoustic Doppler flowmetry of axial flow in homogeneous scattering media." Applied Physics Letters 103.9 (2013): 094101.

76. Brunker, Joanna, and Paul Beard. "Velocity measurements in whole blood using acoustic resolution photoacoustic Doppler." Biomedical optics express 7.7 (2016): 2789-2806.

77. Fox, Ryan. "Optimization of a digital clutter filter for microvascular volume quantification using power doppler ultrasound." London, ON: Department of Medical Biophysics, Western University (2012).

78. Bjærum, Steinar, Hans Torp, and Kjell Kristoffersen. "Clutter filter design for ultrasound color flow imaging." IEEE transactions on ultrasonics, ferroelectrics, and frequency control 49.2 (2002): 204-216.

79. Eckart, Carl, and Gale Young. "The approximation of one matrix by another of lower rank." Psychometrika 1.3 (1936): 211-218.

80. Park, Geunyong, *et al.* "New adaptive clutter rejection based on spectral analysis for ultrasound color Doppler imaging: Phantom and in vivo abdominal study." IEEE Transactions on Biomedical Engineering 61.1 (2013): 55-63.

81. Yankeelov, Thomas E., *et al.* "Correlation between estimates of tumor perfusion from microbubble contrast-enhanced sonography and dynamic contrast-enhanced magnetic resonance imaging." Journal of Ultrasound in Medicine 25.4 (2006): 487-497.

82. Mezl, M., *et al.* "Quantitative ultrasound perfusion analysis in vitro." Proceedings of Biosignal 2010: Analysis of Biomedical Signals and Images. Vol. 20. Brno University of Technology, 2010.

83. Sohlberg, Sara, *et al.* "Placental perfusion in normal pregnancy and early and late preeclampsia: a magnetic resonance imaging study." Placenta 35.3 (2014): 202-206.

84. Kudomi, Nobuyuki, *et al.* "Non-invasive estimation of hepatic blood perfusion from H2 15O PET images using tissue-derived arterial and portal input functions." European journal of nuclear medicine and molecular imaging 35.10 (2008): 1899-1911.

85. Jerosch-Herold, Michael, *et al.* "Analysis of myocardial perfusion MRI." Journal of Magnetic Resonance Imaging: An Official Journal of the International Society for Magnetic Resonance in Medicine 19.6 (2004): 758-770.

86. Ishida, Masaki, *et al.* "Absolute blood contrast concentration and blood signal saturation on myocardial perfusion MRI: estimation from CT data." Journal of Magnetic Resonance Imaging: An Official Journal of the International Society for Magnetic Resonance in Medicine 29.1 (2009): 205-210.

87. Berzigotti, Annalisa, *et al.* "Evaluation of regional hepatic perfusion (RHP) by contrast-enhanced ultrasound in patients with cirrhosis." Journal of hepatology 55.2 (2011): 307-314.

88. Calamante, Fernando, Peter J. Yim, and Juan R. Cebral. "Estimation of bolus dispersion effects in perfusion MRI using image-based computational fluid dynamics." Neuroimage 19.2 (2003): 341-353.

89. Sourbron, S. P., and David L. Buckley. "Tracer kinetic modelling in MRI: estimating perfusion and capillary permeability." Physics in Medicine & Biology 57.2 (2011): R1.

90. Fieselmann, Andreas, *et a*l. "Deconvolution-based CT and MR brain perfusion measurement: theoretical model revisited and practical implementation details." International Journal of Biomedical Imaging 2011 (2011).

91. Kanda, Tomonori, *et al.* "CT hepatic perfusion measurement: comparison of three analytic methods." European journal of radiology 81.9 (2012): 2075-2079.

92. Fan, Ching-Hsiang, *et al.* "Contrast-enhanced ultrasound imaging for the detection of focused ultrasound-induced blood-brain barrier opening." Theranostics 4.10 (2014): 1014.

93. Di Carli, Marcelo F., *et al.* Clinical myocardial perfusionPET/CT." Journal of Nuclear Medicine 48.5 (2007): 783-793.

94. Kambadakone, Avinash R., and Dushyant V. Sahani. "Body perfusion CT: technique, clinical applications, and advances." Radiologic Clinics of North America 47.1 (2009): 161-178.

95. Bleeker, Hendrik, K. Shung, and J. Barnhart. "On the application of ultrasonic contrast agents for blood flowmetry and assessment of cardiac perfusion." Journal of ultrasound in medicine 9.8 (1990): 461-471

96. Chen, Jian-Feng, *et al.* "Autocorrelation of integrated power Doppler signals and its application." Ultrasound in medicine & biology 22.8 (1996): 1053-1057.

96. Wear, Keith A., and Richard L. Popp. "Methods for estimation of statistical properties of envelopes of ultrasonic echoes from myocardium." IEEE transactions on medical imaging 6.4 (1987): 281-291.

97. Alder, B. J., and T. E. Wainwright. "Decay of the velocity autocorrelation function." Physical review A 1.1 (1970): 18.

98. Jia, Yali, *et al.* "Split-spectrum amplitude-decorrelation angiography with optical coherence tomography." Optics express 20.4 (2012): 4710-4725.

99. Esenaliev, Rinat O. "Optoacoustic monitoring of physiologic variables." Frontiers in Physiology 8 (2017): 1030.

100. Pollard RE, Dayton PA, Watson KD, et al. Motion corrected cadence CPS ultrasound for quantifying response to vasoactive drugs in a rat kidney model. Urology. 2009;74(3):675–81

101. Aoudi, W., et al. "Estimation methods for flow imaging with high frequency ultrasound." Ultrasonics 44 (2006): e135-e140.

102. Fox, Ryan. "Optimization of a digital clutter filter for microvascular volume quantification using power doppler ultrasound." London, ON: Department of Medical Biophysics, Western University (2012).